Downloaded from http://sp.lyellcollection.org/ by guest on February 14, 2019

Accepted Manuscript

Geological Society, London, Special Publications

Remote Sensing applications in the Fars Region of the Zagros Mountains of Iran

Jorge Ginés, Rowan Edwards, Tina Lohr, Hayley Larkin & Rachel Holley

DOI: https://doi.org/10.1144/SP490-2018-147

Received 2 August 2018
Revised 24 January 2019
Accepted 28 January 2019

© 2019 The Author(s). Published by The Geological Society of London. All rights reserved. For permissions: http://www.geolsoc.org.uk/permissions. Publishing disclaimer: www.geolsoc.org.uk/pub_ethics

To cite this article, please follow the guidance at https://www.geolsoc.org.uk/onlinefirst#how-to-cite

Manuscript version: Accepted Manuscript
This is a PDF of an unedited manuscript that has been accepted for publication. The manuscript will undergo copyediting, typesetting and correction before it is published in its final form. Please note that during the production process errors may be discovered which could affect the content, and all legal disclaimers that apply to the book series pertain.

Although reasonable efforts have been made to obtain all necessary permissions from third parties to include their copyrighted content within this article, their full citation and copyright line may not be present in this Accepted Manuscript version. Before using any content from this article, please refer to the Version of Record once published for full citation and copyright details, as permissions may be required.

Downloaded from http://sp.lyellcollection.org/ by guest on February 14, 2019

Remote Sensing applications in the Fars Region of the Zagros Mountains of Iran.

abbreviated title: Remote Sensing in Fars (Zagros)

Jorge Ginés[1*], Rowan Edwards[1], Tina Lohr[2], Hayley Larkin[1] and Rachel Holley[1]

1 – CGG NPA Satellite Mapping – Crockham Park, Edenbridge, TN8 6SR (United Kingdom)

2 – ERCE – 2, Cherry Orchard Road, Croydon, CR0 6BA (United Kingdom)

*Corresponding author (e-mail: jorge.gines@cgg.com)

ACCEPTED MANUSCRIPT

ABSTRACT

The Zagros Mountains in Iran are an active fold-and-thrust belt that contains world class examples of folding and salt tectonics. The Fars Region is an excellent location for testing remote sensing methods and applications of satellite data due to its dry climate and superb exposure of geological features. Recent advances in satellite technology and image acquisition have resulted in high quality global datasets at increasing resolution that provide a highly valuable source of data for structural analysis of fold-and-thrust belts. Oblique lineaments like the Razak Line in eastern Fars can be identified by changes in the dimensions of anticlines, presence of deflected folds, offsets in the alignment of structures, location of anticlinal plunges and exposures of salt. Drainage analysis can show propagation and coalescence of anticlines. We review several methods using optical data, digital elevation models, and interferometric synthetic-aperture radar. We integrate those methods and generate detailed geological maps, structural cross-sections, identify structural steps and hidden basement features, and compare to seismological data and their effect on the exposed geology.

The Zagros Mountains are a geologically active fold-and-thrust belt resulting from the convergence between Arabia and Eurasia, and has been subject of much geological research due to its economic potential as an important hydrocarbon province, and the captivating geology and tectonic processes

Downloaded from http://sp.lyellcollection.org/ by guest on February 14, 2019

that have shaped it. The semi-arid climate and poor chemical weathering makes the Zagros a natural laboratory for Earth observation research.

The Zagros have caught the eye from orbit since the first astronauts were equipped with cameras in space. As early as 1966 the Gemini 12 mission acquired photographs of the Fars Province in Iran and the Oman Peninsula, like the one reproduced in figure 1. This image already unveils in detail the large anticlines following the trend of the Fars Arc and many exposed diapirs. The low incidence angle of the sun highlights NE-SW striking lineaments in eastern Fars, near Qoshm Island.

The term remote sensing was first used in the 1950s by Evelyn L. Pruitt at the U.S. Navy's Office of Naval Research, as she recognized that the term 'aerial photography' no longer accurately described the many forms of imagery collected outside the visible region of the electromagnetic spectrum (Campbell 1996). Remote sensing is of particular interest in young fold-and-thrust belts, as they form challenging (and often inaccessible) terrains, with good geological exposure of recent structures. The interpretation of satellite data provides valuable information that can be used to create geological maps, cross-sections and other geological tools that help to understand the tectono-stratigraphic evolution of an area of interest and describe its geological features.

Despite this, remote sensing is often not fully integrated in the workflow of geological exploration. One of the reasons can be that these methods are often not explained beyond remote sensing literature, and exploration geologists may not be fully aware of the different possibilities that remote sensing offers to them.

Recent advances in satellite technology have resulted in high-quality and high-resolution commercial imagery and data which are very valuable for geological research. Commercial products can provide sub-metric resolution for optical imagery (e.g. sensors like WorldView-3 & -4, Pleiades, Kompsat-3A and SuperView-1), 5 m resolution digital elevation models (e.g. AW3D), and metric and sub-metric resolution radar imagery (e.g. RADARSAT-2 and TerraSAR-X). However, it is not always practical for technical and economic reasons to use such high-resolution datasets. Non-commercial options, provided by space agencies like NASA, ESA and JAXA, are the optimal solution for regional exploration projects, as they cover wider areas at a resolution of 10-15 m/pixel in the case of optical data (e.g. Landsat 7 ETM+, Landsat 8 OLI, Sentinel-2), and up to 30 m resolution for digital elevation models (e.g. SRTM-1 and AW3D-30) and radar data (e.g. Sentinel-1, ENVISAT).

The aim of this paper is to present and describe a series of remote sensing applications and techniques of value in the exploration of fold-and-thrust belts using examples from Fars in the Zagros Mountains. These techniques are applicable in most geological contexts. We focus on the production of geological maps from the photo-interpretation of satellite images, the extraction of dip values from digital elevation models, the construction of geological cross-sections using the previous information and well-established geometrical methods, the geometrical analysis of folds, the analysis of topography, drainage patterns and river topographic profiles, and finally, the application of InSAR data to estimate surface deformation and related fault mechanisms.

We use the results of our analysis to discuss the interaction between basement structures and sedimentary cover, a topic that has been subject of previous research by numerous authors (e.g. Fürst 1990; McQuillan 1991; Barzegar 1994; Berberian 1995; Hessami *et al*. 2001; Talebian & Jackson 2004, Leturmy et al. 2010; Di Cuia et al. 2017), and how remote sensing techniques can help unravel the style and kinematics of basement involved structures. The location of the examples used throughout this article is shown in figure 2.

ACCEPTED MANUSCRIPT

Downloaded from http://sp.lyellcollection.org/ by guest on February 14, 2019

Geological Background

The Zagros orogen is a 2000 km long mountain range that extends from south-eastern Turkey through Syria, Iraq and Iran to the Strait of Hormuz. The orogen is divided into three parallel tectono-stratigraphic zones, from NE (hinterland) to SW (foreland): the Urumieh-Dokhtar magmatic assemblage (UDMA), the Sanandaj-Sirjan Zone (SSZ), and the Zagros Fold-and-Thrust Belt (ZFTB). The latter is the focus of this study and is the significant hydrocarbon province with world-class reservoirs (e.g. Bordenave & Hegre 2010; Cooper 2010; Aldega *et al.* 2014). The Zagros Fold-and-Thrust Belt is further subdivided into High Zagros (Imbricated Zone) and Simply Folded Zone (or Simply Folded Belt), which are separated by the High Zagros Fault, and constrained to the SSZ by the Main Zagros Reverse Fault (figure 3). The Mountain Front Flexure is a topographic feature of the Zagros Fold-and-Thrust Belt, rather than a fault in the surface, and separates the Simply Folded Belt from the outer lowlands where younger structures are hidden under Neogene sediments (Alavi 2007).

Embayments (also known as recesses) and salients shape the Simply Folded Zone and cause tectonic compartments with different lithostratigraphic sequences: Kirkuk and Dezful Embayments, Lorestan (Pusht-e Kuh Arc), Izeh Zone and Fars Arc (figure 3). Fault zones oblique to the ZFTB create further partitions, along which anticlines deflect or change their strike direction, or show Hormuz Salt at the surface. Most of those fault zones are N-S striking, and many of them are highlighted on figure 3: Kazerun Fault, Kareh Bas Fault, Izeh Fault, Sabz Pushan Fault. Their presence is probably related to inherited basement structures that controlled sediment deposition during the Mesozoic and Cenozoic, and act as lateral ramps or transfer faults during recent compressional tectonics (e.g. Alavi 2004; Sepehr & Cosgrove 2004; Bahroudi & Talbot 2006; Lacombe 2006; Di Cuia & Pace 2017). Fars has developed complex structural styles due to the presence of isolated salt diapirs prior to Neogene shortening (Letouzey & Sherkati 2004; Jahani *et al*. 2009; Duffy *et al*. 2018). The low taper of the fold-and-thrust-belt, equal or less than 1º in the Fars Arc, is related to the presence of Hormuz Salt (Molinaro et al. 2005).

Numerous authors have described the geology and tectonics across the Zagros region in great detail (e.g. James & Wynd 1965; Stocklin 1968; Berberian & King 1981; Alavi 1994, 2004 & 2007; Stampfli 2000; Hessami 2002); hence we give here only a very brief summary based on those authors. The mountain belt formed as a result of collision between the Arabian and Eurasian plates following the subduction of their interposed oceans. Exposed rocks are predominately shallow to deep marine sediments, continental shelf deposits, volcanic rocks and ophiolites, as well as serpentinites and radiolarites.

The regional stratigraphy of the Fars Arc is shown in figure 4 together with lateral lithological variations and major tectonics events. The Zagros Fars region is characterized by multiple tectonic events: rifting and opening of the Neo-Tethys during the Permo-Triassic, subduction of Neo-Tethys oceanic plate underneath the Iranian lithosphere during Early to Late Cretaceous times, obduction of oceanic slivers during the Late Cretaceous, and collision during the Cenozoic to recent times.

Cenozoic compressional tectonics are responsible for the present-day shape of the orogen and resulted in thickening through buckling and thrusting of a 12 to 15 km thick Phanerozoic sedimentary cover over a regional decollement of thick Precambrian–Cambrian Hormuz Salt, especially in the Fars and Dezful areas. The sedimentary cover is composed of Paleozoic, Mesozoic, and Cenozoic sediments of alternating competent and incompetent layers. Variations in thickness and distribution of the Hormuz Salt and intermediate detachment layers (e.g. Triassic evaporites) result in differential fold-and-thrust propagation throughout the Zagros Belt (Sepehr & Cosgrove 2004), as the detachment layers act as a primary control in the structural style of the basin deformation.

Little is known about Paleozoic to early Mesozoic rocks of the sedimentary cover and their structural configuration due to the lack of exposure and poor seismic imaging. Permo-Triassic rifting and opening of the Neo-Tethys Ocean created accommodation space for a thick sequence of platform and

ACCEPTED MANUSCRIPT

Downloaded from http://sp.lyellcollection.org/ by guest on February 14, 2019

shelf deposits. These were later deformed and became part of the Zagros Fold-and-Thrust Belt. Rifting was likely associated with normal faulting, however, there is no clear evidence for extensional faults, mainly due to the lack of outcrops of Permo–Triassic units. Indirect evidence comes from focal mechanism data (figure 5) of present-day seismicity that show NW-SE striking high-angle reverse faults and sub-vertical strike-slip faults. Most of the earthquakes are located above the basement, at uncertain depths, and coseismic surface faulting is very rare (Talebian & Jackson 2004). Berberian (1995) highlighted that earthquake depths can be constrained to the lower part of the sedimentary cover and delineate the major basement faults that divide the major tectonic provinces of the Zagros Mountains. Teleseismically registered focal mechanism data are associated with high uncertainty in their depth range, hence the sedimentary cover to basement boundary is not well constrained. High-angle reverse faults are interpreted as Permo-Triassic normal faults that have been inverted during present-day compressional tectonics (Jackson & Fitch 1981; Sepehr & Cosgrove 2004). Unlike other fold-and-thrust belts (e.g. Bolivian Sub-Andes), the Zagros Fold-and-Thrust Belt is seismically active with some degree of coupling along the Hormuz Salt detachment and basement involvement via blind reverse faults or thrusts (e.g. Berberian 1995). Areas where seismicity occurs just above the basement in the lower sedimentary cover (figure 5) are often located underneath areas where changes in the topography can be observed, e.g. changes in the strike or size of anticlines, uplifted terraces, vertical and lateral steps in the drainage pattern (Berberian 1995).

In the classical models of fault-bend folding (Suppe 1983) and fault-propagation folding (Suppe & Medwedeff 1990), anticlines develop long backlimbs that are parallel to an underlying thrust ramp. The lack of this morphology and the absence of large thrusts and reverse faults in the surface geology of the Simply Folded Zone in Fars, points to the predominance of detachment folds that formed above well constrained detachment levels (e.g. Precambrian–Cambrian Hormuz, Triassic Dashtak, Miocene Gascharan) that are extensively documented (e.g. Najafi *et al.* 2014; Jahani *et al.* 2009). Published seismic data (Najafi *et al.* 2014) also support the predominance of detachment folds, often showing reverse faults on the flanks and accommodating shortening after the fold has developed, as recent models of fault-propagation folding over listric faults predict (Cardozo & Brandenburg 2014). Beyond the High Zagros Fault, the High Zagros Belt is characterized by strongly deformed overthrust anticlines mainly composed of autochthonous Jurassic-Cretaceous outcrops with Paleozoic cores along numerous reverse faults (Berberian 1995). The variation in structural style from the High Zagros to the Simply Folded Zone in eastern Fars is summarized as a regional cross-section in figure 6, and further discussed in the 'cross-section construction' method later in this article.

ACCEPTED MANUSCRIPT

Satellite data

There are three main types of satellite data for Earth observation purposes: optical images, which are produced from reflected light at various wavelengths and emitted thermal infrared, digital elevation models, that represent the elevation of the terrain, and radar data, which records the reflected signals from a transmitted microwave source.

There are many options in terms of the spatial resolution of the data. Commercial products offer better resolution than open access datasets: WorldView-3 & -4 offer optical imagery at 30 cm resolution, and Pleiades, Kompsat-3A and SuperView-1 all offer 50 cm resolution; digital elevation models like AW3D provide 5 m resolution, and stereoscopic optical imagery can be used to produced digital elevation models of 1 m per pixel; commercial radar products like RADARSAT-2 provide 1 m resolution, whereas TerraSAR-X can produce imagery at 25 cm resolution.

Non-commercial options, provided by space agencies like NASA, ESA and JAXA, are usually free to access or available at low cost. They are in the range of 10 to 15 m resolution for optical data (e.g. Landsat 7 & 8, Sentinel-2), 30 m for digital elevation models (e.g. SRTM-1, AW3D-30), and 30 m for radar data (e.g. ENVISAT, Sentinel-1). This range of resolution is usually sufficient for regional

Downloaded from http://sp.lyellcollection.org/ by guest on February 14, 2019

projects. The examples in this article have all been created using open access imagery and satellite data that we describe in the next subsections.

Optical data

An RGB (red, green and blue) image is formed by choosing three bands that control each of the primary colours of the image. A natural colour image is therefore rendered by mixing the red, green and blue bands in their respective channels. But this is only one of many possible alternatives. More often geologists use other band combinations that highlight spectral characteristics of the rocks beyond the visible region of the electromagnetic spectrum, creating false colour composites. Given the number of bands that satellites like Landsat or Sentinel-2 provide, there are hundreds of potential band combinations. In practice, only a handful of band combinations are usually considered for a semi-arid region such as the Zagros. The examples shown in this article have been produced using Sentinel-2 bands 12, 8 and 3, such as those shown in figure 7.

Landsat. The Landsat program of the National Aeronautics and Space Administration (NASA) began in 1972 with the launch of Landsat 1, and to this date is the longest running satellite imagery acquisition program of Earth. It is currently managed by the United States Geological Survey (USGS). Landsat 1 carried the Multi-Spectral Scanner (MSS), a sensor that provided 80 m resolution in the visible and two near-infrared (NIR) bands. Landsat 4 was launched in 1984 and, together with the MSS sensor of its predecessors, it carried the Thematic Mapper (TM) sensor, providing 30 m resolution imagery in the visible, the NIR and in the shortwave infrared (SWIR). It also included a 120 m resolution thermal IR (TIR) band, resampled to 30 m. Landsat 7 was launched in 1999 with the Enhanced Thematic Mapper+ sensor (ETM+) that includes a panchromatic band that allows resampling of the visible and thermal bands to 15 m resolution. Landsat 8 was launched in February 2013, with the Operational Land Imager (OLI) and Thermal Infrared Sensor (TIRS) instruments, and provides visible, NIR and SWIR, resampled to 15 m and TIR bands resampled to 30 m. Landsat 9, identical to Landsat 8, is expected to be launched in 2020.

Sentinel. The Sentinel constellation of satellites is part of the Copernicus programme of Earth observation of the European Commission. Sentinel-2a was launched in June 2015 and Sentinel-2b followed in March 2017. They provide wider optical scenes than Landsat (swath width of 290 km vs 185 km for Landsat), and a higher resolution (10 m/pixel) for the visible and near-infrared bands. Sentinel-2 images provide excellent quality, both spectral and spatially.

ASTER. The Advanced Spaceborne Thermal Emission and Reflection Radiometer (ASTER) is a multispectral imager developed by the Japanese Space Agency (JAXA) and was launched aboard the Terra satellite of NASA in December 1999 (Nikolakopoulos *et al*. 2006). ASTER offers 14 multispectral bands, with a spatial resolution of 15 m in the visible and near infrared (VNIR), 30 in the SWIR and 90 m in TIR. The infrared bands of ASTER are commonly used in mapping alteration minerals and onshore seep detection, applications beyond the purpose of this paper. The VNIR data, acquired with a stereo telescope, produce the digital elevation model we will briefly describe in the next section.

ACCEPTED MANUSCRIPT

Downloaded from http://sp.lyellcollection.org/ by guest on February 14, 2019

Digital elevation models (DEM)

Digital elevation models (DEM) provide basic information on heights of the Earth's surface and features upon it (Hirt *et al*. 2010). DEMs are usually displayed as a pseudo-colour image and shading computed from the DEM draped over, in order to create a realistic visualization of the terrain that assist the interpretation of structural elements.

SRTM. The Shuttle Radar Topography Mission (SRTM) radar system launched aboard the Space Shuttle Endeavour (mission STS-99) in February 2000, and during the 10 days that the mission lasted acquired topographic data over nearly 80% of Earth's land surface using Interferometric Synthetic Aperture Radar (InSAR) (Nikolakopoulos *et al*. 2006).

SRTM DEM provides two global datasets (see comparison in figure 8): SRTM-3 (3 arcseconds or approximately 90 m resolution), and SRTM-1 (1 arcseconds resolution or approximately 30 m resolution). Both datasets were released to the public between 2004 and 2005, but SRTM-1 was only available initially for areas within the United States. In 2014 it was released globally. SRTM has been an example of engineering at its best (Farr *et al*. 2007), and still today is a fundamental topographic dataset for regional-to-license block geological studies due to its reliability, availability and ease of use.

ASTER GDEM. The stereoscopic capabilities of the optical ASTER data allowed the creation of the ASTER GDEM, or Global DEM. Its first version was released in June 2009, and covered 99% of the landmass of Earth; GDEM v2 was released in 2011. Global DEM has not surpassed the use of SRTM due to quality issues, as it contains several artefacts and errors that limit its applications.

AW3D-30. The Japan Aerospace Exploration Agency (JAXA) released the AW3D-30 digital elevation model (1 arcsecond, approximately 30 m resolution), free of charge in May 2015, generated from the 5 m resolution commercial dataset. The improvement of AW3D-30 over SRTM1 is remarkable, as figure 8 shows, and we strongly recommend its use in geological mapping, topographic/river analysis, and other applications, expecting it to be the fundamental DEM of choice for regional studies.

InSAR

Radar data was first acquired for Earth Observation purposes 40 years ago. Since then there have been multiple missions collecting Synthetic Aperture Radar (SAR) data for mapping and monitoring applications, such as SRTM. Radar data has two components; intensity, which can be used for structural mapping, and phase which can be used for ground deformation monitoring.

Regular data acquisitions on a global scale began with the European Space Agency (ESA) ERS satellites from 1991 onwards. These were followed by Envisat ASAR between 2002 and 2012, and Sentinel-1 from 2014, in addition to a variety of higher-cost commercial satellites. These sensors each provide C-band radar data (5.6 cm wavelength), at approximately 30 m spatial resolution in their standard acquisition mode. The Sentinel-1 satellites now provide routine acquisitions across all global land areas every 12 days (or more frequently), with open access data available to download within 24 hours of acquisition.

ACCEPTED MANUSCRIPT

Downloaded from http://sp.lyellcollection.org/ by guest on February 14, 2019

Archives of SAR data make it possible to derive retrospective measurements. SAR images contain information about the position of ground and structures at the time of image acquisition. As subsequent images are acquired over a single location, phase difference images, termed interferograms are created to reveal measurements of relative terrain motion. This principle forms the basis of InSAR measurements. For more information regarding InSAR the reader is referred to Bamler and Hart (1998), Rosen *et al*. (2000) and Hanssen (2001).

Remote sensing applications and methods

The geological interpretation of aerial photographs and satellite data has contributed to the exploration of resources and the enhanced understanding of every region on our planet. Remote sensing techniques facilitate the geological mapping of mineral deposits, structural features, lithological units, and virtually any element exposed at the surface. Satellite data is in many cases the only available method of exploration in areas of political conflict or in frontier exploration provinces.

The application that is perhaps most commonly associated with remote sensing in the field of exploration is the development of geological maps. The analysis of remotely sensed data facilitates their creation and increases the efficiency of the mapping process, as it allows the coverage of large areas with highly accurate data at a low cost.

Geological mapping

Geological elements are identified in optical satellite images by their tone, pattern, texture, scale, shape or context (Drury 2001) in the same way they have been traditionally identified in aerial photographs. Different rock types respond to weathering and erosion in different ways, depending on their composition and degree of lithification (Drury 2001). In Zagros, a typical sub-arid zone, physical weathering is more prominent than chemical processes because rainfall is limited. Topography is often controlled by lithology, and it is common for cliff-forming limestones, such as the Asmari, Jahrom or Bangestan units, to form topographic highs.

A simple way of adding a topographic effect to an optical image is to overlay the shading computed from a digital elevation model with some transparency (as it has been done in figure 2) This process has the advantage of offering composites with shadows of any length and direction, as the shading is calculated artificially from the DEM. A drawback of this method is the lower resolution of the final result due to the DEM having usually less resolution than the optical data that it masks. A better way of enhancing the relief of a scene is to choose the right season/time of the year: choosing scenes acquired during Spring or Autumn when the shadows are not too short to flatten the image nor too long to cover the surface features we want to identify. Autumn images also benefit from less vegetation after the dry season which would otherwise mask surface features (figure 7).

The mineralogical composition controls the spectral signature of the surface materials, and therefore how a particular rock is depicted in a satellite image. For example, ferrous minerals and hydroxides control absorption at 0.9 μm; albedo of common rocks peaks around 1.6 μm; OH^- minerals have absorption at 2.1 to 2.2 μm, and carbonates commonly absorb at 2.35 to 2.4 μm (Drury 2001; Campbell 1996). For this reason, spectral band combinations, used in order to produce false colour images, are a powerful tool that highlights minerals and helps to detect different types of rocks by their composition.

Faults are recognized by their linear nature. However, there are many ways in which recognizable linear features may be formed, such as stratigraphic contacts, dykes, roads, fluvial streams, or image acquisition and processing artefacts. Many faults are directly visible on optical imagery, simply

ACCEPTED MANUSCRIPT

Downloaded from http://sp.lyellcollection.org/ by guest on February 14, 2019

because they cause colour changes in the data at both sides of the fault, or by their shadow when they produce some topographic effect. Faults are also often inferred from the presence of vegetation that grows along the fault zone, as they act as water pathways or aquifers. Some faults cause topographic steps large enough to be visible on a DEM. Faults can have an impact on fluid circulation and cause changes in vegetation, which can result in textural changes of the surface.

Folds are recognized by changes in bedding dip direction. The landscape in Fars is populated by numerous large 'whaleback' anticlines (i.e. well developed and elongate double plunging folds with a concentric crest) where resistant cliff-forming carbonates are exposed at the surface. In areas where topographic features have been eroded, folds can be more difficult to identify, for example in areas where Agha Jari is the exposed unit at the surface.

Figure 7 shows a comparison of three different Sentinel-2 composites for the area between the Dehnow and the Gazeh Anticlines. The first two images (a and b) are made by combining bands 12, 8, 3 (SWIR, NIR and green) as red, green and blue, in order to produce false colour images. Image (a) corresponds to data acquired in early June 2018, while the data for image (b) was acquired in early October 2017. The longer shadows of the second composite enhance the topography and therefore the structure. Anticlines are better defined and their asymmetry is clearer, particularly in the Gazeh Anticline. Erosional elements are more visible and minor fractures in carbonates, like those developed in the Cretaceous Bangestan limestones, are more evident too. Nevertheless, the first composition is useful as it shows the lithological contacts more neatly, and we would recommend using both as they fulfil different purposes.

The same autumn scene is used to produce the third composite (c), but in this case as a natural colour rendition (4, 3, 2 band composition). Although natural colour images better represent what the human eye would perceive in the field, many lithological differences are masked. The Jurassic to Cretaceous Khami Group limestones in the core of the Dehnow Anticline appear in red in the first two composites and contrast well with the green tones of the Cretaceous Bangestan Group, however this difference is much more subtle in the natural colour composition (c) and it would be difficult to map their contact accurately using this image. Such differences are due to varying mineralogical compositions, which the false colour composition depicts better as those differences are more noticeable in the infrared bands used. Another example is the contrast between the Miocene Gascharan evaporites and Mishan carbonates: they are teal and light grey in the false colour composition, while they are both very similar in the natural colour image.

DEMs are also a fundamental part in the geological mapping workflow. They can be easily displayed as pseudo-colour images that are so familiar in Earth sciences, where a colour palette represents elevation values (Drury 2001). DEMs provide topographic information that assists the interpretation of structural relationships, allowing the detection of structures by their topographic expression. Often, this expression is very subtle and optical data alone cannot show it. DEM data can also display different textural patterns that may correspond to different rock types.

An example of a geological map produced from an optical satellite image is shown in Figure 9. We have used a Sentinel-2 12, 8, 3 band combination from a scene in October 2017 (a) to produce the geological map (b) containing a series of large anticlines in eastern Fars. The NE-SW strike of the Kuh-e Shu Anticline (or Shab Anticline) contrasts with the general E-W strike of other folds in this region, such as the Kuh-e Anguru, Kuh-e Handun and Kuh-e Gashu. These major anticlines are topped by grey Guri marls which surround the Gascharan evaporites, recognized by their bright teal tones. The Guri Member develops very distinctive flat irons particularly in the Kuh-e Anguru Anticline. Flat irons are triangular shaped landforms with a steep and uniform dip slope, and are a typical erosional pattern between rocks of different resistance. They can provide a visual indication of the asymmetry of an anticline, as occurs in the Kuh-e Anguru, where these landforms are steeper at the southern flank than they are at the northern limb.

ACCEPTED MANUSCRIPT

Downloaded from http://sp.lyellcollection.org/ by guest on February 14, 2019

Below the Gascharan Formation are the grey-brownish coloured Asmari limestones, and farther underneath, the Pabdeh–Gurpi carbonates and Bangestan Limestones, as can be seen in the Kuh-e Anguru and the Kuh-e Shu anticlines.

There are many diapirs in this area that reach the surface by breaching the hinges of anticlines. The diapirs appear in dark red to brown colour, they are formed by disorganized blocks of Hormuz Salt and can therefore be recognized by their irregular and chaotic surface.

The band composition of figure 9 (a) shows very distinctive purple tones which represent Agha Jari and Mishan clastic sediments that form the synclines together with resistant conglomerates of the Bakhtiari Formation.

Leturmy *et al*. (2010) interpret the NE-SW strike of the Kush-e Shu structure as a rotation related to contractional tectonics and reverse faulting of a basement structure. They support this interpretation with several observations, including a higher crestal profile and deeper stratigraphic level exposed at Kuh-e Shu in comparison to its continuation along strike, the Kuh-e Gashu Anticline, and several topographic indicators that we discuss in later sections. They estimate a basement step of c. 1500 m related to reverse faulting, which other authors explain by strike-slip faulting along the basement fault (e.g. Hessami *et al*. 2001) or by coalescence of growing anticlines (e.g. Ramsey *et al*. 2008)

Dip data extraction

Dip values can be measured from a DEM by extracting the spatial coordinates of three coplanar points of a bed or stratigraphic contact. Those coordinates are then used to resolve the 3-point problem of structural geology.

Most Geographic Information Systems (GIS) assist this process with strike and dip calculation tools. Figure 10 shows the script included with *TNT Mips* in action, all calculated points must be validated by an interpreter. When a quantitative measurement is not possible (i.e. in flat landscapes or when the stratigraphy is subvertical), it is always possible to estimate relative dips (e.g. sub-horizontal, shallow, gentle, moderate, steep, subvertical). Manual extraction of dip and dip direction values is an easy and very fast method. In areas of optimal exposure and stratigraphic control of the topography, as occurs in Zagros, hundreds of values can be estimated in a few hours. Accurate dip values and detailed definition of stratigraphic boundaries allows the calculation of real thicknesses of lithostratigraphic units.

The example in figure 10 shows several dip and strike measurement calculated in the northern flank of the Kuh-e Anguru anticline, which benefit from the extraordinary development of flat irons in the Guri limestone above the Gascharan evaporites.

Fold analysis

The analysis of exposed anticline geometries can be greatly valuable in predicting subsurface geology, including folding mechanisms and depth to the detachment, and has been the object of previous publications in the area (e.g. Ramsey *et al*. 2008; Burberry *et al*. 2010; Leturmy 2010).

The exposed anticlines of the Fars region are mainly ’whaleback‘ double-plunging anticlines, with typical lengths ranging from 20 to 50 km, and widths from 5 to 12 km. The anticlines follow the curved trace of the Fars Arc often with small lateral offsets between fold structures as they continue along strike. The largest of these offsets are caused by deep-seated lineaments cross-cutting the Fars region. Koyi *et al.* (2016) modelled such basement lineaments with three different deformation

ACCEPTED MANUSCRIPT

Downloaded from http://sp.lyellcollection.org/ by guest on February 14, 2019

scenarios. A key observation of their models is the discrepancy in the apparent surface trace of basement faults and their actual location at depth. The offset between both emphasizes the importance of using a variety of techniques to clearly delineate these features. Additionally, these lineaments can cause deflections of folds at surface without actual offset, e.g. the Kuh-e Shu anticline (figure 9). Similar features occur in other parts of Zagros, such as Kurdistan (Di Cuia *et al*. 2016; De Vera *et al*. 2009)

Using a fold classification scheme based on Hudlestone (1973), the surface expression of folds seen on digital elevation models such as SRTM-1 or AW3D-30 can be used to describe folds in an objective and easy way. The majority of anticlines in Fars range from a B2 geometry with a broad axial region and steep limbs, through to a D2 geometry, having a narrower fold hinge and slightly shallower dipping limbs, whilst maintaining a comparable amplitude. They could also be described as Class 1C folds based on the classification of Ramsay (1967). This information can be valuable in the construction of cross-sections or interpretation of seismic data.

Anticlines have often grown interfering with neighbouring folds, by coalescing along strike, or forming pairs of structures roughly parallel to each other (Ramsey 2008). Alternatively, a fold may have grown into a cross-strike structure caused by a basement structure (Leturmy *et al.* 2010; Di Cuia & Pace 2017). In some places smaller anticlines have developed on the flank of larger anticlines, e.g. Dehnow Anticline (See 'Cross-section construction').

The Razak Line is a N-S striking lineament that defines the eastern boundary of the Gavbandi High in Coastal Fars (see figure 3 for location), where the Precambrian–Cambrian Hormuz Salt is assumed to be thinner than in adjacent areas (Talbot and Alavi 1996; Farzipour-Saein & Koyi 2016). The thickness variation of Hormuz Salt can be inferred by the lack of surface diapirs on the Gavbandi High, (figure 3), and published seismic data (e.g. Najafi *et al*. 2014).

We have quantified the geometry of outcropping anticlines around the Razak Line (figure 11), with the primary aim of calculating their length-to-width ratio which expresses their eccentricity, or slenderness, and their spatial distribution. Their dimensions have been obtained by measuring the length and the width of the outermost clearly exposed unit of each anticline, usually coincident with their topographic expression. Measurements are consistent between most anticlines, but there are uncertainties where anticlines are exposed at different levels or grow adjacent to each other, however the resulting change in the ratio measurement is acceptable. The Kuh-e Shu Anticline illustrates this: Using its topographic extent the measured ratio is 4.13, but when using a unit consistently visible around the full extent of the structure, such as the Asmari, yields a ratio of 4.66. This variation of around 12% is consistent across structures and is an acceptable error for illustrative purposes.

The length-to-width ratios of the anticlines (figure 11) are generally lower east of the Razak Line than west of it. This is quantified in the plots in figure 12 which illustrate the ratio vs. length relationship (figure 12a) and the width vs. length relationship (figure 12b). Both plots show a distinctive distribution of each of the clusters on either side of the Razak Line. Plot a) emphasizes that anticlines of a similar length have a greater spectrum of ratios in the west (3 to 11) than in the east (2 to 7), i.e. for a given length anticlines are generally wider on the eastern region. Plot b) shows that the anticlines in the east have lengths between 15 and 50 km are always wider than 5 km (and up to 16 km), whereas a width of 5 km is a typical value for many anticlines in the west. In other words, anticlines west of the Razak Line have typically smaller widths and are therefore slenderer in comparison to the less eccentric anticlines found on the eastern region, where anticlines can grow longer and wider at the same time (i.e. their ratio does not increase as much as in the east).

This variation on either side of the Razak Line seems to be controlled by the presence of an intermediate decollement, the Triassic Dashtak Formation (Farzipour-Saein & Koyi 2016), which limits the amount of growth of an anticline above the regional, and hence, their width, to smaller sizes than the deeper Hormuz Salt does, as the literature on detachment folding predicts (Jamison 1987; Bulnes

ACCEPTED MANUSCRIPT

Downloaded from http://sp.lyellcollection.org/ by guest on February 14, 2019

& Poblet 1999). The data might indicate first and second order anticlines west of the Razak Line: first order anticlines are those that show low ratios and detach on Hormuz Salt, whereas second order anticlines are the ones with higher ratios and detach on Dashtak evaporites. Second order anticlines are generally abstent east of the Razak Line due to the dominance of Hormuz Salt and a preference for low-ratio first order anticlines. This is reflected in the cross-sections described in the following section and figure 13.

There are uncertainties when applying this method to a small population as it is relatively susceptible to errors in the measurements of the anticlines, particularly when their topographic expression can be variable. However, it provides regional information about the variation of detachment levels, folding styles, and it can highlight the presence of basement structures controlling the deformation of the sedimentary cover.

Cross-section construction

By carefully defining the dip domains and lithological thicknesses of fold structures one can predict and construct cross-sections, using the dip domain construction technique. The method is based on the assumption that the beds occur as planar segments separated by narrow hinges (Groshong 2006), and beds can be drawn concentric to each other. The fold analysis explained above can assist to predict detachment levels and the general geometry of anticlines in profile view.

We show two short cross-sections in figure 13 modified from Farzipour-Saein & Koyi (2016). Unit thickness, dip angles and dip directions, as well as stratigraphic contacts have been measured and mapped from Sentinel-2 images and AW3D-30 DEM. The same method and the same data have been used to produce the regional cross-section included in figure 6, from Bandar Abbas to the Sanandaj-Sirjan Zone.

Cross-sections A and B are constructed at both sides of the Razak Line in order to show the variation of structural style. Section A is located to the west of the Razak Line and shows the Dehnow anticline, the eastern termination of the Varavi anticline, and the Beyram anticline. Section B, located to the east of the Razak Line, shows the Gavbast and Bavush anticlines. Both sections are characterized by large detachment anticlines above the Hormuz Salt. In this interpretation the anticlines on the eastern section present reverse faults at their frontal limbs that accommodate part of the deformation as the folds grow when shortening by folding becomes increasingly more difficult.

The lesser thickness of Precambrian–Cambrian Hormuz Salt in the western cross-section triggers the intermediate detachment of the Triassic Dashtak Formation and causes lower-amplitude folds within the post-Triassic sedimentary cover, as we have explained in the previous section. Folds formed above these units are typically narrower, as the position of the decollement is higher. They are also more asymmetric, with longer backlimbs and steeper front limbs, suggesting a fault-propagation folding mechanism for these relatively shallow anticlines. This has been replicated with analogue models and discussed by Farzipour-Saein & Koyi (2016). These lower-amplitude folds form above deeper high-amplitude anticlines that developed as detachment anticlines along the Hormuz Salt, but the reduced Hormuz Salt thickness seems to inhibit further fold propagation. On the eastern side of the Razak Line, the high thickness of the basal decollement (i.e. Hormuz Salt) dominates the folding style and causes the whole sedimentary cover to deform harmonically (Farzipour-Saein & Koyi 2016).

The regional cross-section in figure 6 has been constructed using a geological map derived from the interpretation of Landsat 8 imagery and AW3D-30 DEM. A series of faulted detachment anticlines have developed above Hormuz Salt in the Simply Folded Zone (i.e. Suru, Genau, Handun, Finu). To the north of the Faraghun Anticline, in the High Zagros, the structural style is characterized by fault-bend folds that accommodate most of the shortening in the region. A large fault-bend-fold is

ACCEPTED MANUSCRIPT

Downloaded from http://sp.lyellcollection.org/ by guest on February 14, 2019

interpreted beneath the Main Zagros Reverse Fault. More locally, imbricates and duplex systems form in the Jahrom Fm, as the flat-ramp-flat thrusts transfer deformation stratigraphically upwards from the hinterland (Molinaro *et al*. 2005); very similar structures have been described in regions of other fold-and-thrust belts, such as the Ždánice Nappe of the Carpathian Mountains (Poul *et al.* 2011). Late stage out-of-sequence thick-skin reverse faults dissect previous structures of the fold-and-thrust belt (Molinaro *et al*. 2005). The structure of the Simply Folded Zone in our section has been modified from Jahani *et al*. (2009), whereas the structure of the High Zagros and the basement has been adapted from Molinaro *et al*. (2005). We assume a 'layer cake' approach at this regional scale, as Mesozoic and Paleozoic subsidence rates are very low (Sharland *et al*. 2001; Molinaro *et al*. 2005).

Geomorphic analysis

The applications described so far are based on the interpretation and the analysis of exposed structures. However, in many onshore provinces in the world, where topography is low and the sedimentary infill has obscured deeper structures (Berger 1994), geomorphic analysis become a very useful and accessible tool. Regional topographic and river profiles can be derived from global DEMs such as SRTM and AW3D30. The analysis of subtle changes in the topography of a fold-and-thrust belt, and the analysis of the drainage pattern and river profiles can indicate the presence of buried and obscured structures, as deep as basement involved faults (see Leturmy *et al*. 2010).

Topography. The four topographic profiles in figure 14 have been extracted from the 30 m resolution AW3D-30 DEM. The profiles are 300 km long each, and their orientation is approximately parallel to the tectonic transport. They start in the Persian Gulf (left side of the profiles) and terminate in the hinterland of Zagros. Individual anticlines form high-frequency elements along the profiles, which can be up to 1500 m higher than the surrounding alluvial planes. The anticlines at the front of the Simply Folded Zone and at the front of the High Zagros Zone cause the largest contrast in the surrounding landscape.

The profiles show a broader pattern of first order features that reflect regional changes in topography and coincide with major zone boundaries (e.g. High Zagros Fault, Mountain Front Flexure, Main Zagros Reverse Fault) or other basement related faults, implying that deformation in the internal parts of the fold-and-thrust belt is still ongoing. The topographic steps separate segments that are typically between 50 and 80 km long. Each segment presents a very low taper angle, and the overall elevation gain towards the hinterland is fundamentally caused by the uplift produced along the topographic steps.

Profile (a) in figure 14 shows steps at 45, 140, 175, 230, and 280 km from the origin of the profile in the Persian Gulf. These steps coincide with the positions of the Mountain Front Flexure, the Kareh Bas Fault, the Sabz Pushan Fault, Kuh-e Ahmadi (a large anticline just south of the High Zagros Fault) and, finally, the Neyriz Ophiolite thrust. Similar steps and segmentations are seen in the other three profiles. The step caused by the High Zagros Fault is particularly pronounced in profiles (3) and (4). Intermediate steps that may be associated with basement structures like the Bastak Basement Fault and the Shu Basement Fault are visible at 105 km in profile (3) and at 130 km at the location of the Muran Anticline in profile (d). Major basement structures seem to be segmented in branches. Finally, these topographic profiles also show the migration of the vertical uplift between different branches when they are organized in an en-echelon array.

Drainage pattern. The drainage network in Zagros is relatively young and developed during the last few million years when the fold-and-thrust belt emerged from a marine environment to terrestrial conditions (Leturmy *et al*. 2010). The rivers form a trellis pattern that is controlled by structural and lithological weaknesses. The main rivers form long valleys that follow synclines, whereas small

ACCEPTED MANUSCRIPT

Downloaded from http://sp.lyellcollection.org/ by guest on February 14, 2019

parallel tributaries flow from the slopes of the anticlines joining the main river segment at a sharp angle.

When rivers cross anticlines they form watergaps. The development of a watergap can be related to the continuous incision of a river through a growing anticline, or to an inactive anticline that is increasingly more exposed by erosion of younger rocks above it (Ramsey *et al*. 2008).

Windgaps, or dry watergaps, are remnant watergaps that have been abandoned as the anticline grows or its exposure increases. Ramsey *et al*. (2008) present an excellent case study of windgap migration and evolution of tributary patterns developed on the slopes of the Kuh-e Handun Anticline (figure 15a).

In any given double plunging fold, an ideal tributary pattern is formed by curved stream courses at the terminations of the fold, and straight downhill courses where the anticline has a cylindrical geometry. In other words, flow follows the maximum slope and is perpendicular to topographic contour lines. Figure 15b shows this distribution in an ideal periclinal fold. When the fold grows in length, developing a cylindrical central segment (figure 15c), the new pattern formed at the terminations is again curved, but in the cylindrical region of the anticline new straight drainage streams develop that may mask the inherited curved pattern (Ramsey *et al*. 2008).

The Kuh-e Handun is pierced in its central part by a diapir of Hormuz Salt. The River Shur approaches the anticline from the north, is then deflected and surrounds the anticline along its western side. It passes by the town of Fin and continues southwards after crossing a ridge of Bakhtiari conglomerates. Two windgaps can be seen at the termination of the anticline (figure 15a): The eastern windgap is higher than the western one, this is likely related to the westward lateral propagation of the anticline and its successive vertical growth. To the east of the windgaps, soft layers of Guri marls have been almost totally eroded, uncovering the much harder Asmari formation. The remnants of Guri limestones preserve an inherited curved stream course pattern that is superimposed by the newer straight streams formed in the deeper Asmari Formation, suggesting an actual growth of the anticline since the region emerged.

River profiles. The concept of *base level* of a river was introduced by J.W. Powell in 1875 (Burbank and Anderson 2001), defining the lower limit of a landscape below which rivers cannot erode. The base level is commonly the river outlet at sea level, but it can also be in local terms the shore of a lake or reservoir, or the joining of a tributary with the main river (Ramsey 2008, Burbank & Anderson 2001). Another important concept in the analysis of river topographic profiles is the *base level of erosion*, defined as the equilibrium longitudinal profile 'below which a stream cannot degrade and at which neither net erosion nor deposition occurs' (Bull 1990; Burbank & Anderson 2001).

River profiles are typically concave, formed by reaches that progressively decrease their slope as the flow advances towards the outlet (Leturmy *et al*. 2010). Deviations from this ideal profile are expressed by knickpoints and development of local convex segments along the profile. These alterations are usually related to vertical tectonic movements of the terrain, changes in the direction of the river, lithological differences in the surface geology, and development of local base levels. A local base level can be caused by the formation of natural or artificial dams, presence of gorges, and by other similar phenomena. Knickpoints are locations where the slope of a stream is steepened with respect to the adjoining segments of the river profile (Burbank & Anderson 2001); they are typically high frequency alterations along the profile of the river, and they occur over a short distance. Leturmy *et al*. (2010) present an analysis of knickpoints and topographic steps in the eastern Fars Region, which we have applied for our analysis.

We have constructed three topographic river profiles using the 30 m resolution AW3D-30 DEM data (figure 16). The three chosen rivers are, from west to east, Mand**,** Mehran and Shur. Mand

ACCEPTED MANUSCRIPT

Downloaded from http://sp.lyellcollection.org/ by guest on February 14, 2019

and Shur flow from the mountains in the High Zagros Zone, while Mehran drains from Coastal Fars in the Simply Folded Zone and flows perpendicular to the coast near the Mountain Front Flexure.

The River Mand is approximately 700 km long and flows from the High Zagros Zone to the Persian Gulf, crossing some of the major structures in the region. The first relevant knickpoint, at 90 km from the origin, indicates a reduction of the slope, which could be caused by a lithology change, or perhaps by the uplift of the High Zagros Zone. At 140 km the river crosses the termination of the Sarvestan Fault, causing another knickpoint, and continues straight towards a narrow valley between the Kuh-e Kaftar and Kuh-e Karbasi Anticlines, shown as a wide knickpoint at 210 km. This alteration in the river profile could be related to diapirism in Kuh-e Kaftar, to the effect of a blind fault underneath, or a combination of both.

At 405 km there is another knickpoint, where the river flows along a tight syncline, formed by resistant Bakhtiari conglomerates. The river then turns at 435 km abruptly towards the coast, crossing the Kuh-e Kolagh Anticline by a watergap. This could be indicating some kind of uplift in the area that forced the river to change its direction at this point.

After another very subtle knickpoint caused by a watergap at 540 km in the area where the Mountain Front Flexure is mapped, the river reaches the coastal alluvial plain, discharging into the Persian Gulf.

The River Mehran flows parallel to the coast, for just over 400 km. The long valley it forms is enclosed between a series of longitudinal alignments of anticlines, connected along strike by saddles and deflections. These trains of anticlines form the longest ranges in Fars. The southern range is more regular and continuous, and it marks the location of the Mountain Front Flexure (figure 3).

The river profile has a moderately concave shape, as the source of the river is at an elevation of just 500 m. There are two clear knickpoints on the profile: one at 185 km from the source, and a less pronounced one at 280 km. The first knickpoint (185 km) is located near the town of Kemeshk, where the river passes between the Gazeh Anticline, to the north, and the Dehnow Anticline, to the south. The Dehnow Anticline forms a longitudinal train of anticlines with the Lavarestan and the Namaki structures, connected by saddles and small offsets. The crest of Dehnow Anticline consists of a large exposure of Mesozoic rocks (Khami and Bangestan Groups). However, the dominant outcropping rocks to the east are the Oligocene-Miocene Asmari (Lavarestan Anticline) and Miocene Gascharan (Namaki Anticline). The structural variation along strike occurs near the knickpoint and suggests that the basement could be deeper to the east than to the west, which is consistent with the interpretation of Leturmy *et al*. 2010 for the Kuh-e Shu Anticline. Both areas are located along a lineament interpreted by Barzegar (1994) as the Shu Basement Fault (see topographic profiles of figure 14).

The second knickpoint (280 km) appears between the Herang salt diapir to the south, and the Kuh-e Nakh anticline to the north, where the river flows through a narrow valley after passing a relatively wide alluvial plain. There are similar features to those described at the first knickpoint: The Kuh-e Nakh and Kuh-e Baviyun structures form another longitudinal train of anticlines where the rocks exposed at Kuh-e Nakh are older than at Kuh-e Baviyun, suggesting again that the location of the knickpoint is related to a deeper fault in the basement. This fault, like others in the area, is also recognized by Barzegar (1994).

Ramsey *et al*. (2008) identify several windgaps dissecting the southern train of anticlines that bounds the valley of the river Mehran, indicating where the river discharged to the sea in the past, showing a migration of the river mouth from east to west.

The River Shur flows from the High Zagros Zone to the Qoshm Straight in the Persian Gulf for 480 km, and terminates near the mouth of the River Mand. The first knickpoint is at 80 km from the source, where the river changes its direction from transversal to longitudinal to the structures, which is

ACCEPTED MANUSCRIPT

Downloaded from http://sp.lyellcollection.org/ by guest on February 14, 2019

associated to a change to a lower slope angle. From there, the river flows parallel to the High Zagros Thrust, and crosses it at least twice, i.e. 100 and 220 km. The most remarkable change occurs at 310 km as the river crosses the Kuh-e Muran Anticline. This knickpoint, and other smaller points down the driver, seem to be more recent than others, as the change is more abrupt and the base level of erosion is not yet in equilibrium. Once again, this knickpoint is located along a lineament that has been interpreted as a suspected basement fault by previous authors (Barzegar 1994).

Leturmy *et al*. (2010) interpret several knickpoints, topographic steps, diapir alignments and topographic changes in the shape of major folds as evidence for a NE-SW basement step causing an uplift of the block at the northwest. Barzegar (1994) interprets the same structure from Landsat MSS images as the Shu Basement Fault.

Interferometry

Drainage patterns and river profiles allow us to study the cumulative influence of tectonics over long periods of time, but satellite data can also use very short-term events to derive insight into the subsurface structure. Surface deformation from earthquake events can be measured using satellite InSAR, giving valuable information on the location, depth and orientation of the fault slip.

Satellite InSAR is a remote sensing technology that involves the interferometric processing of multi-temporal (time-lapse) SAR images acquired by earth observation satellites to detect, map and monitor surface deformation. It is capable of remotely detecting millimetres to metres of deformation spanning multi-temporal periods (days to decades), across specific sites or wide areas with a scale ranging from tens to thousands of square kilometres.

Archives of SAR data make it possible to derive retrospective measurements. SAR images contain information about the position of ground and structures at the time of image acquisition. As subsequent images are acquired over a single location, phase difference images, termed interferograms, are created to reveal measurements of relative terrain motion. This principle forms the basis of InSAR measurements. For more information regarding InSAR the reader is referred to Bamler and Hart (1998), Rosen *et al*. (2000) and Hanssen (2001).

The example in figure 17 uses Envisat ASAR data to derive surface displacement between 29/12/2005 and 18/05/2006, spanning the March 2006 Fin earthquake in the south eastern part of the Simply Folded Zone. Although InSAR only reveals deformation at the surface, the characteristics of this surface deformation pattern can be used to reveal information about the earthquake fault, and therefore the structure at depth.

In this example, each colour cycle ‘fringe’ can be thought of as a contour showing 2.8 cm of increasing displacement towards the satellite, i.e. predominantly uplift. Visual examination of the InSAR fringe pattern can infer slip on NE to SW striking fault, and the lack of sharp discontinuities indicates no significant surface rupture.

The InSAR displacements can also be used to constrain a numerical model, to derive estimates for fault parameters such as strike, dip, and slip distribution. Notably, modelling for this earthquake performed by Roustaei *et al*. (2010) estimated the earthquake ruptured a section of the fault plane between 5.4 and 9.3 km deep, within the lower part of the sedimentary cover between the Hormuz Salt and the Gurpi Marls. This interpretation is consistent with the analysis produced with other methods in this paper and by previous authors (Leturmy *et al*. 2010).

ACCEPTED MANUSCRIPT

Downloaded from http://sp.lyellcollection.org/ by guest on February 14, 2019

Discussion

The Fars Province in the Zagros Fold-and-Thrust Belt is an excellent testing site for the application of remote sensing techniques due to its semi-arid character, dry climate and neotectonics. We have provided an insight to some remote sensing methods using open access satellite data (e.g. Landsat 8 and Sentinel-2 imagery). Most of these techniques are also applicable when higher resolution data (e.g. Quickbird, WorldView, SPOT) is available, and they also apply to aerial photographs. Research published at the end of the previous century already showed the value of satellite imagery in the detection and interpretation of suspected basement structures and major lineaments in Zagros, and their relation with the tectonic evolution of the orogen (e.g. Fürst 1990; McQuillan 1991; Barzegar 1994; Hessami *et al*. 2001).

The production of geological maps in a region like Fars benefits greatly from the interpretation of satellite images showing exposed structures and identifiable lithostratigraphic units. False colour images are the most useful choice of optical imagery, as they can be created in order to highlight specific rock types. Using the 13 bands of Sentinel-2, or 11 bands of Landsat-8, there are virtually hundreds of potential band combinations, but most of them are redundant, and only a handful are typically used. For this study we have chosen Sentinel-2 bands 12, 8 and 3 displayed as RGB images (equivalent to Landsat 7 ETM+ bands 7, 4, 2 and Landsat 8 OLI bands 7, 5, 3), where Gascharan evaporites and Agha Jari clastic beds show very characteristic teal and purple colours, respectively, and they can then be used as marker units during the interpretation and the identification of adjacent units. Carbonates in Fars can also be identified by certain characteristics in their remote sensing signature (e.g. Mishan usually appears lighter than Asmari, whereas Khami often looks more red than Bangestan in our examples. On a real colour composite (bands 4, 3, 2 for Sentinel-2 and Landsat 8) rock types in Zagros can often look too similar and their differentiation can be difficult. Other band combinations are possible and we encourage the reader to experiment and learn the basics of image processing in order to obtain the best possible results for their purpose, as this process takes little time with modern software.

The quality of the exposure of structures and the increasing resolution of digital elevation models allow the explorationist to construct detailed geological cross-sections. As we have shown in the sections parallel to the Razak Line, small variations in apparent thickness and dip values are easily detected and quantified using satellite data, and provide valuable information to infer changes in the subsurface structure. We interpret the presence of narrow anticlines to the west of the Razak Line as structures detached on Triassic Dashtak evaporites. This unit acts as a detachment above major deeper anticlines (this study and Farzipour-Saein & Koyi 2016). The fold analysis we have elaborated for this study also shows predominance of smaller folds, but with higher length-to-width ratios, above the Gavbast High, indicating a thinner Hormuz Salt, as has been previously suggested by Jahani *et al.* (2017).

A common denominator seen in the examples of this study is the relationship between basement faults, structural style and topographic features. There is a direct relationship between knickpoints along river profiles and vertical tectonic movements that can indicate the existence of suspected basement faults. The rivers Mand, Merhan and Shur show the presence of several knickpoints where buried structures deform the topographic surface. A similar effect is observed in topographic profiles perpendicular to the structural trend of the fold-and-thrust belt.

Several NE-SW trending major basement structures are evidenced in the surface geology by deflected folds, offsets in the alignments of anticlines, location of anticlinal plunges and salt diapirs piercing the core of the anticlines (Di Cuia & Pace, 2017; De Vera *et al*., 2009) These cross-strike structures and transverse zones are typically associated with the presence of strike-slip faults and thrust lateral ramps (Di Cuia & Pace 2017). In Fars, vertical offset along those structures, together

ACCEPTED MANUSCRIPT

Downloaded from http://sp.lyellcollection.org/ by guest on February 14, 2019

with earthquake data, support the reverse kinematics of underlying basement faults, which has also been proposed by other authors (e.g. Jackson & Fitch 1981; Berberian 1995, Sepehr & Cosgrove 2004; Leturmy *et al*. 2010). Alternative interpretations suggest basement faults with strike-slip kinematics that cause block rotations and lineaments at the surface that are slightly offset from the location of the basement faults (Hessami *et al.* 2001; Koyi *et al.* 2010). Although this is a plausible interpretation from surface data alone, focal mechanism solutions of recorded seismic events are predominantly of reverse nature (see figure 5), if we assume kinematics has not changed significantly since those basement faults have been reactivated. Reverse faults also better explain the diverse surface expressions of structures like Kuh-e Kush, Kuh-e Muran, Kuh-e Shu and Kuh-e Gashu.

The location of the Fin earthquake, analysed with InSAR data, is coincident with the Shu Basement Fault (figure 18). Barzegar (1994) interpreted this fault on Landsat MSS images as one of several NE-SW trending right lateral strike-slip faults in the Eastern Fars that are evidenced by deflected folds, offsets in the alignments of anticlines, location of anticlinal plunges and salt diapirs piercing the core of anticlines. However, Leturmy *et al*. (2010) suggest an important reverse component for the Shu Fault, due to the estimation of a step in the basement of c. 1500 m. Focal mechanism solutions point to a predominant reverse component with minor strike-slip motion along those lineaments.

Conclusions

We have presented some of the most common remote sensing techniques and their applications in the Zagros Fold-and-Thrust belt.

Optical data, digital elevation models, and InSAR data can be used to analyse, interpret and visualize exposed rocks and structures, and predict subsurface geology. Structural data, such as dip and dip direction, and unit thicknesses, can be measured directly from DEM, providing an inexpensive method to quantify fold geometry, assist further geological analysis and produce geological maps. SRTM-1 and AW3D-30 offer almost global coverage at c. 30 m resolution, facilitating this process in areas of difficult accessibility.

We present a regional cross-section that illustrates the general folding style in eastern Fars, and the interaction between sedimentary cover and basement structures. We also present two cross-sections showing the structural variation on both sides of the Razak Line, likely caused by a lesser thickness of Hormuz Salt to the west of this lineament. To the east, larger anticlines detached on Hormuz Salt characterize the exposed structure; to the west, the lesser thickness of Hormuz Salt in the western cross-section triggers the intermediate detachment of the Triassic Dashtak Formation forming narrower asymmetric anticlines in the units above. The variation in structural style on both sides of the Razak Line is also highlighted by the length/width ratio of its neighbouring anticlines, showing a clear trend on both sides of this structure. This ratio can be used in other provinces and basins to detect buried structures and palaeohighs.

The analysis of the profiles of the rivers Mand, Merhan and Shur show several knickpoints where buried structures deform the topographic surface and indicate the existence of basement faults.

Satellite InSAR is capable of detecting subtle surface deformation related to subsurface structures, e.g. the March 2005 Fin earthquake deformation indicating a reverse fault at the Shu basement structure.

By using the here described freely available remote sensing data it is possible to identify several NE-SW trending major basement structures by analysing surface features like deflected folds, offsets in the alignments of anticlines, location of anticlinal plunges, salt diapirs piercing the core of anticlines.

ACCEPTED MANUSCRIPT

Downloaded from http://sp.lyellcollection.org/ by guest on February 14, 2019

Acknowledgements

We thank CGG NPA Satellite Mapping for permission to publish an extract of a proprietary geological map. We are grateful to NASA for distributing historic astronaut photographs and SRTM data, JAXA for distributing AW3D-30, NASA/USGS Landsat Program for distributing Landsat imagery and NOAA for distributing SRTM15 Plus global bathymetric and elevation data. The European Commission are acknowledged for the Copernicus Program which distributes Sentinel data. TNT Mips is a trademark of Microimages, Inc . We also thank Laura M. Parro and Pablo J. González for their help with GMT scripts. Finally, we thank Paolo Pace and another anonymous reviewer for their comments and suggestions, which helped to improve the manuscript.

References

Alavi, M., 1994. *Tectonics of the Zagros Orogenic Belt of Iran; New Data and Interpretations*. Tectonophysics, **229**, 211-238.

Alavi, M., 2004. *Regional Stratigraphy of the Zagros Fold-Thrust Belt of Iran and its Proforeland Evolution*. American Journal of Science, **304**, 1-20

Alavi, M. (2007). Structures of the Zagros fold-thrust belt in Iran. *American Journal of science*, *307*(9), 1064-1095.

Aldega L., Corrado S., Carminati E., Shaban A., Sherkati S., 2014. Thermal evolution of the Kuh-e-Asmari and Sim anticlines in the

Zagros fold-and-thrust belt: Implications for hydrocarbon generation. Marin and Petroleum Geoscience 57, 1-13.

Bahroudi A. and Talbot C. 2006. The configuration of the basement beneath the Zagros Basin. Journal of Petroleum Geology 26(3), 257-282

Bamler, R., Hart, P., 1998. Synthetic aperture radar interferometry. Inv. Probl., vol. 14, no. 4, pp. R1–R54.

Barzegar, F. (1994). Basement fault mapping of E-Zagros foreland belt, southwest Iran, based on space-borne remotely sensed data. In *Proceeding of the tenth thematic conference on geologic remote sensing, exploration, environment and engineering*.

Berberian, M., 1995. *Master 'blind' thrust faults hidden under the Zagros folds: active basement tectonics and surface morphotectonics*. Tectonophysics, **241**, 193-224

Berberian, M. & King, G. C. P., 1981. *Towards a Paleogeography and tectonic evolution of Iran.* Canadian Journal of Earth Science, **18**, 210-265.

Berger, Z. (1994). Satellite Hydrocarbon Exploration. Interpretation and integration Techniques, Berlin, Heidelberg, New York, London, Paris, Tokyo, Hong Kong.

Bordenave M.L. and Hegre J.A. 2010. Current distribution of oil and gas fields in the Zagros Fold Belt of Iran and contiguous offshore as the result of the petroleum systems. Geological Society, London, Special Publications, 330, 291-353

ACCEPTED MANUSCRIPT

Downloaded from http://sp.lyellcollection.org/ by guest on February 14, 2019

Bosold, A., W. Schwarzhans, A. Julapour, A. R. Ashrafzadeh, and S. M. Ehsani. "The structural geology of the High Central Zagros revisited (Iran)." *Petroleum Geoscience* 11, no. 3 (2005): 225-238.

Bull, W. B. (1990). Stream-terrace genesis: implications for soil development. Geomorphology, 3(3-4), 351-367.

Burbank, Douglas W., and Robert S. Anderson (2011). Tectonic geomorphology. John Wiley & Sons

Burberry, C. M., Cosgrove, J. W., & Liu, J. G. (2010). A study of fold characteristics and deformation style using the evolution of the land surface: Zagros Simply Folded Belt, Iran. *Geological Society, London, Special Publications*, *330*(1), 139-154.

Campbell, J.B. (1996). Introduction to Remote Sensing. 622 pp. Guildford Press

Cardozo, N., & Brandenburg, J. P. (2014). Kinematic modeling of folding above listric propagating thrusts. *Journal of Structural Geology*, *60*, 1-12.

Cooper, M. (2007). Structural style and hydrocarbon prospectivity in fold and thrust belts: a global review. Special Publication-Geological Society of London, 272, 447.

De Vera, J., J. Gines, M. Oehlers, K. McClay, and J. Doski. "Structure of the Zagros fold and thrust belt in the Kurdistan Region, northern Iraq." Trabajos de geología 29, no. 29 (2009).

Di Cuia R. and Pace P. 2017. Strike-Slip Faults vs Lateral Ramps in the Zagros Thrust Belt (NE Iraq): Impacts on HC Potentials. AAPG Geoscience Technology workshop, Muscat, Oman.

Di Cuia, R., Pace, P., Bitonte, R. & Riva, A. (2016) - Hydrocarbon Occurrences and Deformation Styles in the Zagros - A Focus on the Kurdistan and Lorestan HC Provinces. 78th EAGE Conference & Exhibition 2016 Vienna, Austria.

Drury, S. A., (2001). *Image interpretation in geology*. 304 pp. UK: Nelson Thornes.

Duffy, O. B., Dooley, T. P., Hudec, M. R., Jackson, M. P., Fernandez, N., Jackson, C. A. L., & Soto, J. I. (2018). Structural Evolution of Salt-Influenced Fold-and-Thrust belts: A Synthesis and New Insights From Basins Containing Isolated Salt Diapirs.

Farzipour-Saein, A., & Koyi, H. (2016). Intermediate decollement activation in response to the basal friction variation and its effect on folding style in the Zagros fold-thrust belt, an analogue modeling approach. *Tectonophysics*, *687*, 56-65.

Farr, Tom G., Paul A. Rosen, Edward Caro, Robert Crippen, Riley Duren, Scott Hensley, Michael Kobrick et al. "The shuttle radar topography mission." Reviews of geophysics 45, no. 2 (2007).

Fürst, M., 1990. Strike-slip faults and diapirism of the south-eastern Zagros ranges. Proceeding of the Symposium on Diapirism, Bandar Abbas, Hormozgan, Iran, 2, 149-18 1.

Groshong Jr, R. H. (2006). *3-D structural geology* (pp. 305-371). Springer-Verlag Berlin Heidelberg.

Hanssen, R.F., 2001. Radar Interferometry: Data Interpretation and Error Analysis. Dordrecht, The Netherlands, Kluwer.

Hessami, K. (2002). *Tectonic history and present-day deformation in the Zagros fold-thrust belt* (Doctoral dissertation, Acta Universitatis Upsaliensis).

Hessami, K., Koyi, H. A., & Talbot, C. J. (2001). The significance of strike-slip faulting in the basement of the Zagros fold and thrust belt. *Journal of Petroleum Geology*, *24*(1), 5-28.

ACCEPTED MANUSCRIPT

Downloaded from http://sp.lyellcollection.org/ by guest on February 14, 2019

Hirt, C., Filmer, M. S., & Featherstone, W. E. (2010). Comparison and validation of the recent freely available ASTER-GDEM ver1, SRTM ver4. 1 and GEODATA DEM-9S ver3 digital elevation models over Australia. *Australian Journal of Earth Sciences*, *57*(3), 337-347.

Hudlestone, P. J. (1973). Fold morphology and some geometrical implications of theories of fold development. *Tectonophysics*, *16*(1-2), 1-46.

Jackson, J. & Fitch, T., 1981. *Basement faulting and the focal depths of the larger earthquakes in the Zagros mountains (Iran).* Geophys. J. Int., **64**, 561–586.

Jahani, S., Callot, J. P., Letouzey, J., & Frizon de Lamotte, D. (2009). The eastern termination of the Zagros Fold-and-Thrust Belt, Iran: Structures, evolution, and relationships between salt plugs, folding, and faulting. Tectonics, 28(6).

Jahani, S., Hassanpour, J., Mohammadi-Firouz, S., Letouzey, J., de Lamotte, D. F., Alavi, S. A., & Soleimany, B. (2017). Salt tectonics and tear faulting in the central part of the Zagros Fold-Thrust Belt, Iran. *Marine and Petroleum Geology*, *86*, 426-446.

James, G.A. & Wynd, J.G., 1965. *Stratigraphic Nomenclature of Iranian Oil Consortium Agreement Area.* Am. Assoc. Petrol. Geol. Bull., **49**, 2182–2245.

Koyi, H., Nilfouroushan, F., & Hessami, K. (2016). Modelling role of basement block rotation and strike-slip faulting on structural pattern in cover units of fold-and-thrust belts. Geological Magazine, 153(5-6), 827-844.

Lacombe, O., Mouthereau, F., Kargar, S., Meyer, B., 2006. *Late Cenozoic and modern stress fields in the western Fars (Iran): implications for the tectonic and kinematic evolution of central Zagros*. Tectonics **25**,

Letouzey, J., & Sherkati, S. (2004, December). Salt movement, tectonic events, and structural style in the central Zagros fold and thrust belt (Iran). In *Salt-sediment interactions and hydrocarbon prospectivity: 24th Annual Research Conference, Gulf Coast Section, SEPM Foundation* (pp. 444-463).

Leturmy, P., Molinaro, M., & de Lamotte, D. F. (2010). Structure, timing and morphological signature of hidden reverse basement faults in the Fars Arc of the Zagros (Iran). *Geological Society, London, Special Publications*, *330*(1), 121-138.

McQuillan, H., 1991. The role of basement tectonics in the control of sedimentary facies, structural patterns and salt plug emplacements in the Zagros fold belt of Southwest Iran. Journal of Southeast Asian Earth Sciences, 5, 453-463.

Molinaro, M., Leturmy, P., Guezou, J. C., Frizon de Lamotte, D., & Eshraghi, S. A. (2005). The structure and kinematics of the southeastern Zagros fold-thrust belt, Iran: From thin-skinned to thick-skinned tectonics. *Tectonics*, *24*(3).

Najafi, M., Yassaghi, A., Bahroudi, A., Vergés, J., & Sherkati, S. (2014). Impact of the Late Triassic Dashtak intermediate detachment horizon on anticline geometry in the Central Frontal Fars, SE Zagros fold belt, Iran. *Marine and Petroleum Geology*, *54*, 23-36.

Nikolakopoulos, K. G., Kamaratakis, E. K., & Chrysoulakis, N. (2006). SRTM vs ASTER elevation products. Comparison for two regions in Crete, Greece. *International Journal of remote sensing*, *27*(21), 4819-4838.

ACCEPTED MANUSCRIPT

Downloaded from http://sp.lyellcollection.org/ by guest on February 14, 2019

Poul, I., Melichar, R., & Janečka, J. (2011). Thrust tectonics of the Upper Jurassic limestones in the Pavlov Hills (Outer Western Carpathians, Czech Republic). *Geological Society, London, Special Publications*, *349*(1), 237-248.

Ramsay, J. (1967). Folding and fracturing of rocks. McGraw-Hill.

Ramsey, L. A., Walker, R. T., & Jackson, J. (2008). Fold evolution and drainage development in the Zagros mountains of Fars province, SE Iran. *Basin Research*, *20*(1), 23-48.

Rosen, P., Hensley, S., Joughin, I., Li, F., Madsen, S., Rodriguez, E., and Goldstein., R., 2000. Synthetic aperture radar interferometry. Proceedings of IEEE, vol. 88, no. 3, pp. 333–382.

Roustaei, M., E. Nissen, M. Abbassi, A. Gholamzadeh, M. Ghorashi, M. Tatar, F. Yamini-Fard, E. Bergman, J. Jackson, and B. Parsons. "The 2006 March 25 Fin earthquakes (Iran)—insights into the vertical extents of faulting in the Zagros Simply Folded Belt." Geophysical Journal International 181, no. 3 (2010): 1275-1291.

Sharland, P. R., R. Archer, D. M. Casey, R. B. Davies, S. H. Hall, A. P. Heward, A. D. Horbury, and M. D. Simmons. "Arabian Plate Sequence Stratigraphy. GeoArabia, Spec Publ 2, Gulf PetroLink." (2001). Sepehr, M. & Cosgrove, J. W., 2004. *Structural framework of the Zagros Fold-Thrust Belt, Iran*. Marine and Petroleum Geology, **21**, 829-843.

Stocklin, J. (1968). Structural history and tectonics of Iran: a review. *AAPG Bulletin*, *52*(7), 1229-1258.

Suppe, J. (1983). Geometry and kinematics of fault-bend folding. *American Journal of science*, *283*(7), 684-721.

Suppe, J., & Medwedeff, D. A. (1990). Geometry and kinematics of fault-propagation folding. *Eclogae Geologicae Helvetiae*, *83*(3), 409-454.

Stampfli, G. 2000. Tethyan oceans. In: Bozkurt, E., Winchester, J. A. & Piper, J. D. A. (eds) Tectonics and Magmatism in Turkey and the Surrounding Area. Geological Society, London, Special Publications, 173, 1–23.

Talebian, M., & Jackson, J. (2004). A reappraisal of earthquake focal mechanisms and active shortening in the Zagros mountains of Iran. *Geophysical Journal International*, *156*(3), 506-526.

ACCEPTED MANUSCRIPT

Downloaded from http://sp.lyellcollection.org/ by guest on February 14, 2019

Figures

Fig. 1. Astronaut photograph s66-63485, showing SE Fars, Qoshm Island and Oman seen from the Gemini 12 on the 13 November 1966. Courtesy of NASA.

Fig. 2. Landsat 8 composite of the Fars Region of the Zagros Mountains, with overlaid AW3D-30 DEM to highlight the terrain. Polygons with number indicate figures location throughout this article. Landsat 8 courtesy of USGS/NASA Landsat Program; AW3D-30 DEM data ©JAXA.

Fig. 3. Tectonic map showing the different Zagros zones and fault systems. Purple polygons are salt diapirs. MZRF, Main Zagros Reverse Fault; HZF, High Zagros Fault; MRF, Main Recent Fault; KF, BL, Balarud Line; KF, Kazerun fault; IF, Izeh Fault; KBFZ, Kareh Bas Fault Zone; SFZ – Sabz Pushan Fault Zone; NFS, Nezamabad Fault System; RL, Razak Line; SF, Sarvestan Fault. Modified from Berberian (1995). Topographic shading from SRTM data courtesy of NASA.

Fig. 4. General chronostratigraphic chart of the Zagros Fold-and-Thrust Belt. Modified from Sepehr and Cosgrove (2004), Alavi (2004), Blanc (2004) and Bosold (2005).

Fig. 5. Teleseismic focal mechanism solutions in the area of study, from the CMT catalogue, from 1970 to 2015. The cross-section view shows solutions projected at depth from a buffer zone 60-km wide at both sides of the transect. Most of the events are resolved as reverse faults, thrust, and strike-slip faults. Seismicity is well distributed in the area, with some areas less active in the hinterland. Major surface lineaments and faults seem to be related with clusters of higher activity. MZRF, Main Zagros Reverse Fault; HZF, High Zagros Fault; MFF, Mountain Front Flexure. Topography and bathymetry calculated from SRTM15 Plus, courtesy of NOAA.

Fig. 6. Regional schematic cross-sections showing the general structure of Zagros in eastern Fars from Bandar Abbas in the Persian Gulf to the hinterland. (a) shows a geological map (modified from a proprietary interpretation of NPA Satellite Mapping) interpreted from Landsat 8 imagery and AW3D-30 DEM. The cross-section portrays a series of large detachment anticlines developed above Hormuz Salt in the Simply Folded Zone, whereas a fault-bend folding style characterizes the High Zagros. Basement structures control the deformation in the sedimentary cover. Modified from Molinaro *et al*. (2005) and Jahani *et al.* (2017). MZRF, Main Zagros Reverse Fault; HZF, High Zagros Fault; MFF, Mountain Front Flexure Landsat 8 courtesy of USGS/NASA Landsat Program; AW3D-30 DEM data ©JAXA. Geological interpretation © CGG / NPA Satellite Mapping.

Fig. 7. Three different Sentinel-2 images to illustrate band composition and time of acquisition differences. (a) and (b) are both false-colour composites (bands 12,8,3) that highlight mineral difference amongst lithological units; however, (a) has been acquired in early summer, and (b) during autumn, providing longer shadows. These effects are useful to better recognize structure. (c) is a real colour composition from the same data as (b), and the lithological differences as poorly recognized in this case. Copernicus Sentinel data 2017 – 2018.

ACCEPTED MANUSCRIPT

Downloaded from http://sp.lyellcollection.org/ by guest on February 14, 2019

Fig. 8. Comparison of (a) SRTM3 (c. 90 m resolution), (b) SRTM1 (c. 30 m resolution) and (c) AW3D-30 (30 m resolution). The open access AW3D-30 DEM is distributed by JAXA and it is the result of downsampling the 5 m resolution original DEM, producing a better defined and more clear DEM than SRTM1 even though both datasets have the same spatial resolution. SRTM data courtesy of NASA; AW3D-30 data ©JAXA.

Fig. 9. Example of a geological interpretation (b) produced from a Sentinel-2 12,8,3 band composition image (a) around Kuh-e Shu in Eastern Fars. Copernicus Sentinel data 2017.

Fig. 10. Example of dip extraction from AW3D-30 DEM using the TNT Mips GIS software. The example is in the northern flank of Kuh-e Anguru. AW3D-30 data ©JAXA. TNT Mips is a trademark of Microimages, Inc.

Fig. 11. DEM highlighting anticlinal structures in Fars. Length and width of each anticlinal segment has been measured, and length vs. width ratios calculated. Green points show ratios from 1 to 3.99, purple 4 and higher. RL, Razak Line; NFS, Nezamabad Fault System. SRTM elevation data courtesy of NASA.

Fig. 12. Plots showing anticline length versus length-to-width ratios (a) and length versus width east and west of the Razaq line.

Fig. 13. (a) Location of the cross-sections A and B around the Razak Line in Fars in a 3D view of a geological map (modified from a proprietary interpretation of NPA Satellite Mapping) produced from Landsat 8 imagery and AW3D-30 DEM. Section A, to the west of the Razak Line, depicts the Dehnow, Varavi and Beyram anticlines. Section B contains the Bavbast and the Bavush anticlines. Sections modified from Farzipour-Saein and Koyi (2016). Landsat 8 courtesy of USGS/NASA Landsat Program; AW3D-30 DEM data ©JAXA. Geological interpretation © CGG / NPA Satellite Mapping.

Fig. 14. Topographic profiles across Zagros. Yellow markers indicate topographic steps. HZF – High Zagros Fault; MFF, Mountain Front Flexure; MZRF, Main Zagros Reverse Fault; NT, Neyriz Thrust; KB, Kareh Bas Fault; SB, Sabz Pushan Fault; BBA, Bastak Basement Fault; SBF, Shu Basement Fault; AA, Ahmadi Anticline; BA, Bandobast Anticline; BuA, Bundasht Anticline; JA, Jahrom Anticline; MA, Muran Anticline. Topography and bathymetry extracted from SRTM15 Plus, courtesy of NOAA.

Fig.15. River profiles of the rivers Mand, Mehran and Shur. Yellow markers indicate relevant knickpoints described in the text. Abbreviations as in fig. 14. . MZRF, Main Zagros Reverse Fault; HZF, High Zagros Fault; MFF, Mountain Front Flexure. Topography and bathymetry extracted from SRTM15 Plus, courtesy of NOAA.

ACCEPTED MANUSCRIPT

Downloaded from http://sp.lyellcollection.org/ by guest on February 14, 2019

Fig 16. (a) Sentinel-2 12,8,3 band composition showing drainage elements in Kuh-e Handun. Two windgaps (white markers) indicate the migration of the River Shur as the anticline grows. Drainage patterns in the Jahrom Fm and the Guri Mb also indicate growth of the anticline. Red markers indicate fractures. Modified from Ramsey *et al*. (2008). (b) Drainage pattern development, showing an ideal pericline (left) where streams form curved paths in the terminations, and a growth anticline (right) where the inherited curved paths coexist with newly formed straight paths. Modified from Ramsey *et al*. 2008. Copernicus Sentinel data 2017.

Fig. 17. Extract from Envisat interferogram 29/12/2005 and 18/05/2006 spanning the March 2006 Fin earthquake. Fringe cycles from blue through yellow to red indicate increasing uplift towards the centre of the displacement zone, measured as motion along the satellite line of sight (LOS). Interferogram © CGG / NPA Satellite Mapping. Envisat data © ESA 2006.

Fig.18. Major river knickpoints and topographic steps coincide with major lineaments mapped from Landsat MSS images by Barzegar (1994). White circle indicates the interferogram of figure 17. RL, Razak Line; NFS, Nezamabad Fault System; HZF, High Zagros Fault; MZRF, Main Zagros Reverse Fault; MFF, Mountain Front Flexure. Salt diapirs are drawn in purple. SRTM elevation data courtesy of NASA.

ACCEPTED MANUSCRIPT

Downloaded from http://sp.lyellcollection.org/ by guest on February 14, 2019

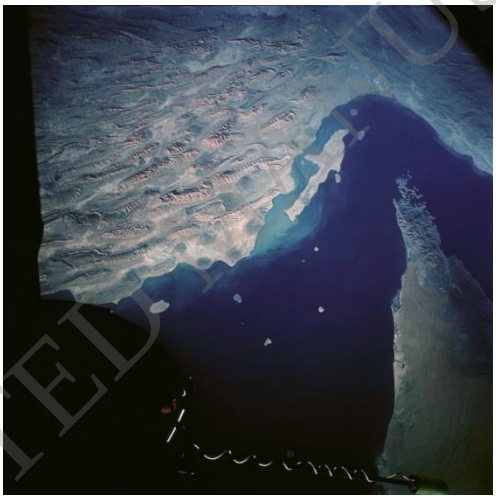

ACCEPTED MANUSCRIPT

Downloaded from http://sp.lyellcollection.org/ by guest on February 14, 2019

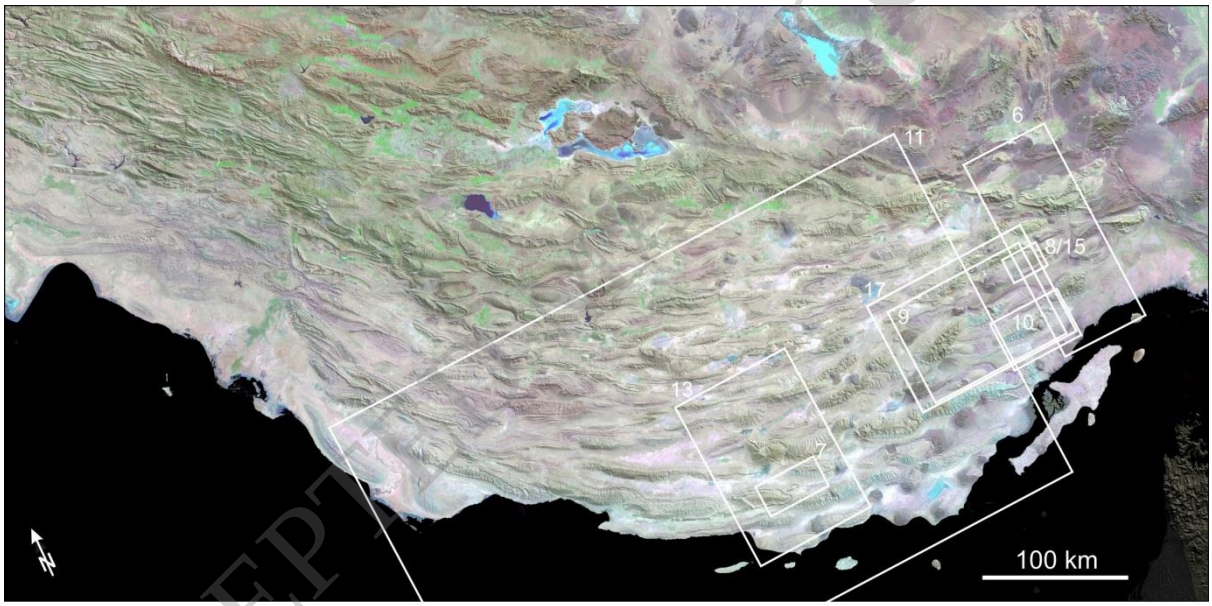

ACCEPTED MANUSCRIPT

Downloaded from http://sp.lyellcollection.org/ by guest on February 14, 2019

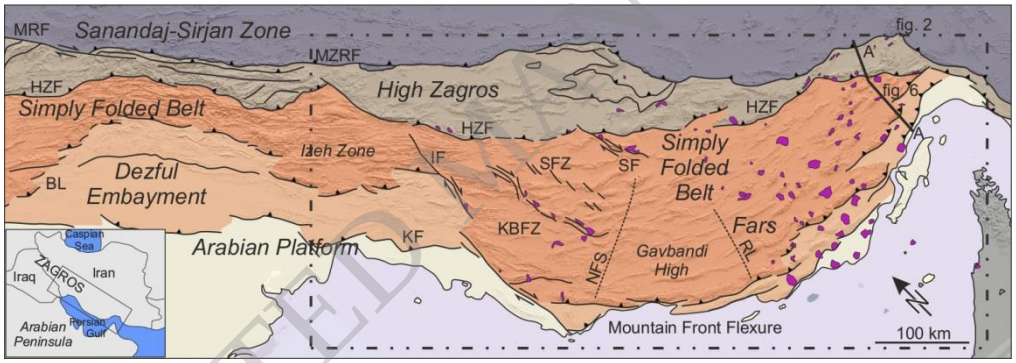

ACCEPTED MANUSCRIPT

Downloaded from http://sp.lyellcollection.org/ by guest on February 14, 2019

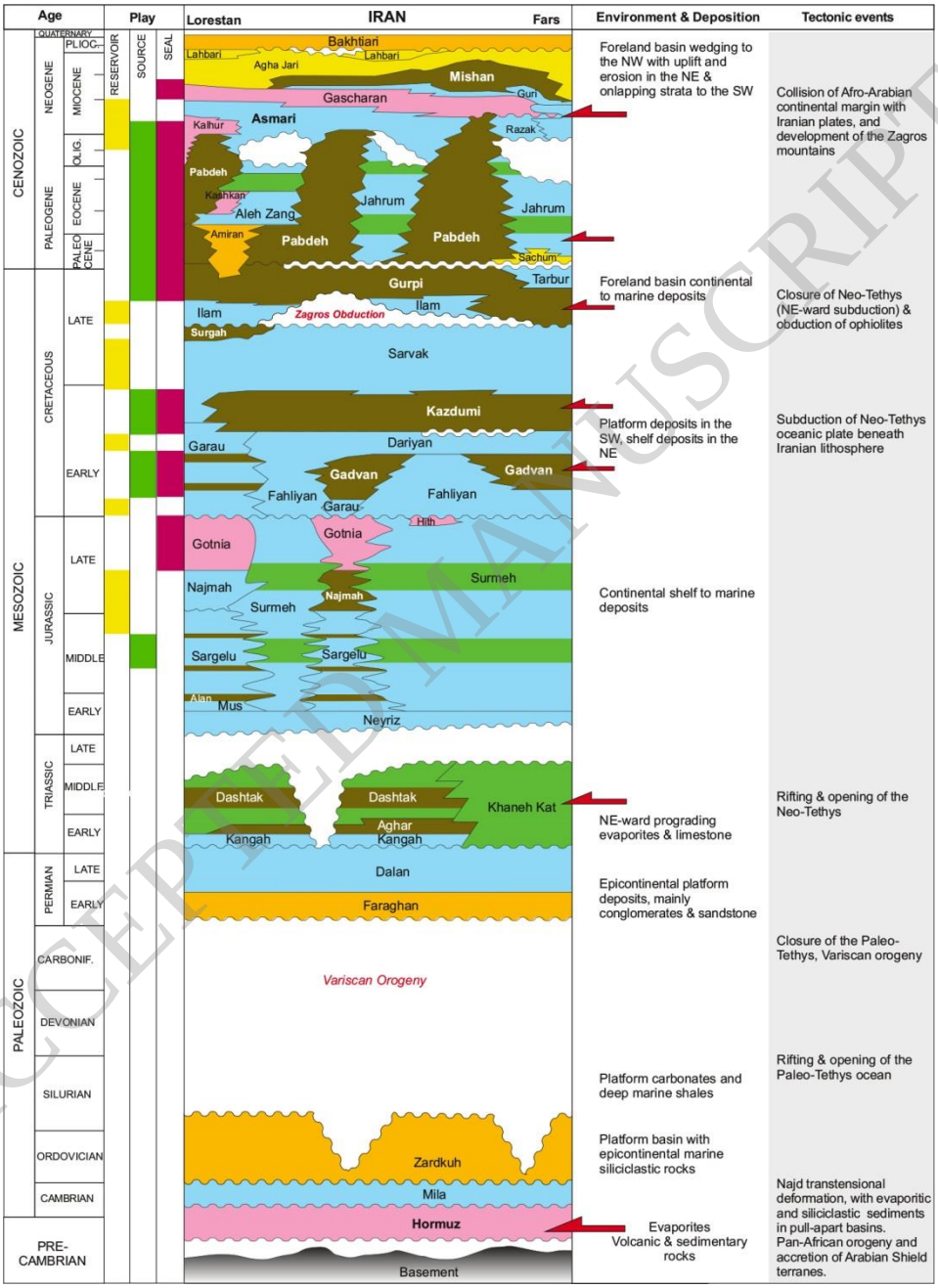

ACCEPTED MANUSCRIPT

Downloaded from http://sp.lyellcollection.org/ by guest on February 14, 2019

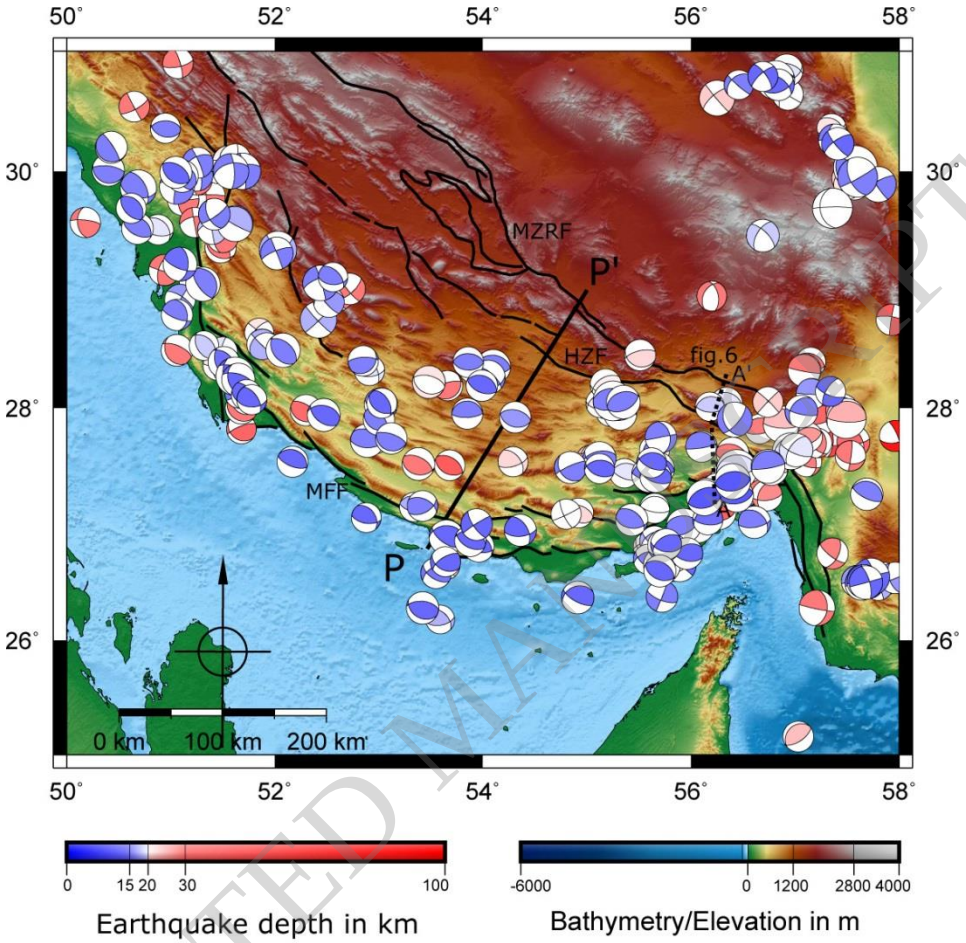

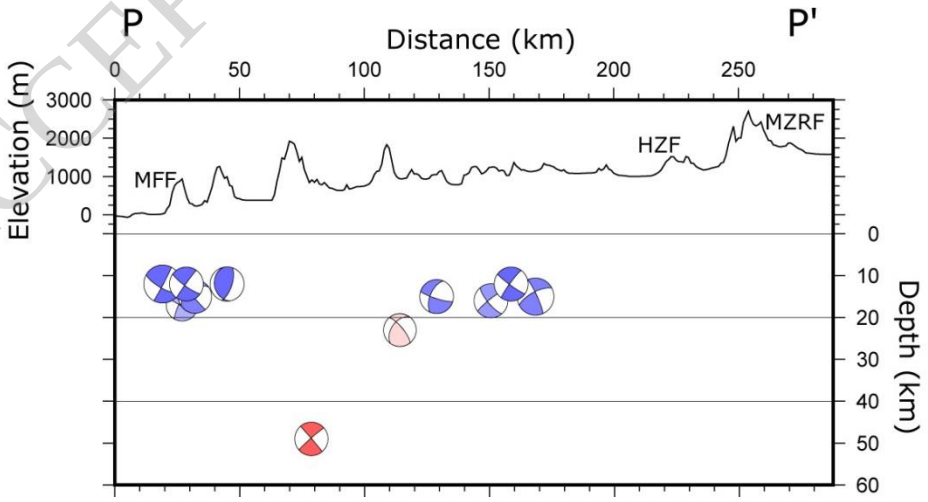

ACCEPTED MANUSCRIPT

Downloaded from http://sp.lyellcollection.org/ by guest on February 14, 2019

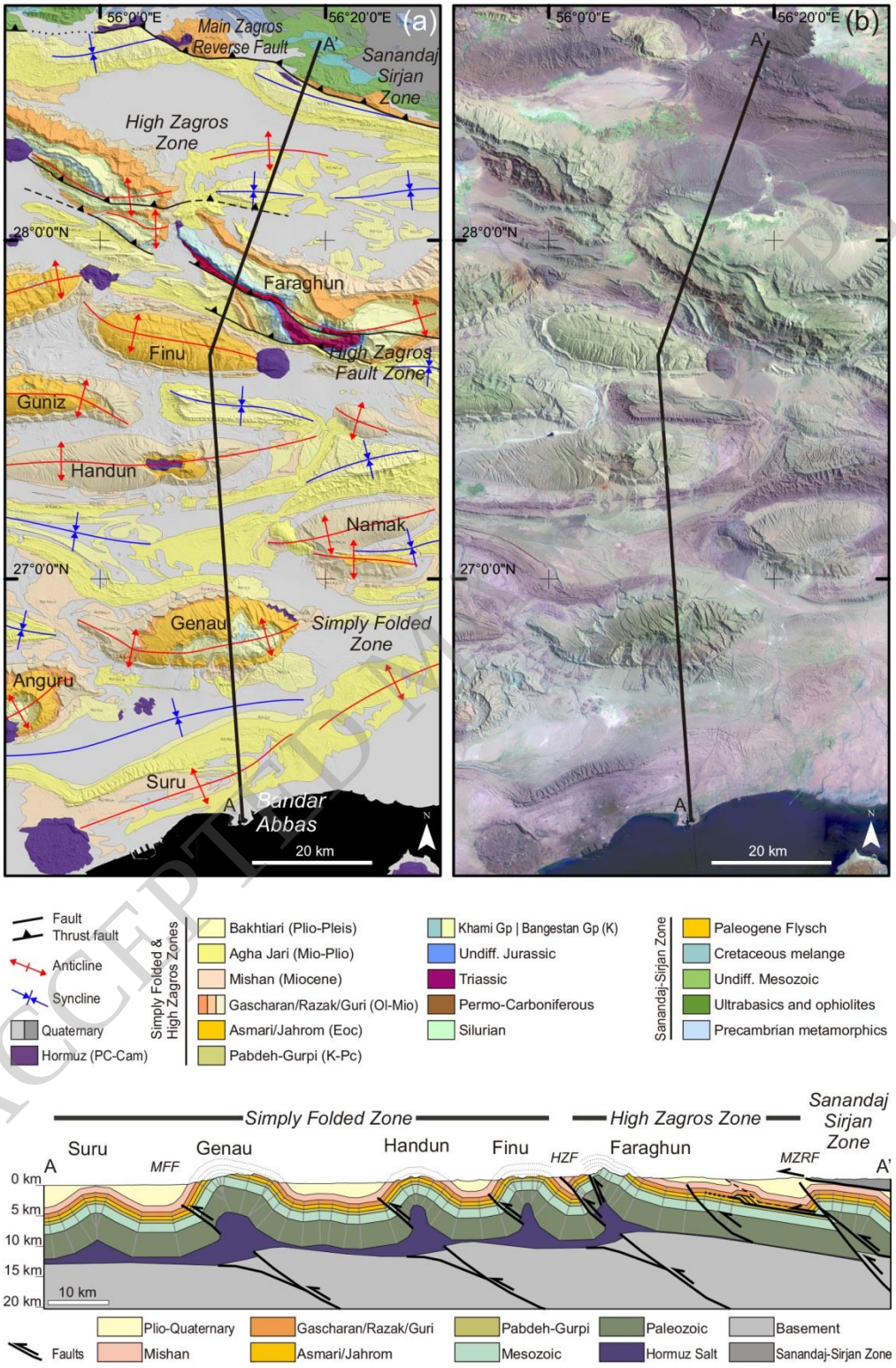

ACCEPTED MANUSCRIPT

Downloaded from http://sp.lyellcollection.org/ by guest on February 14, 2019

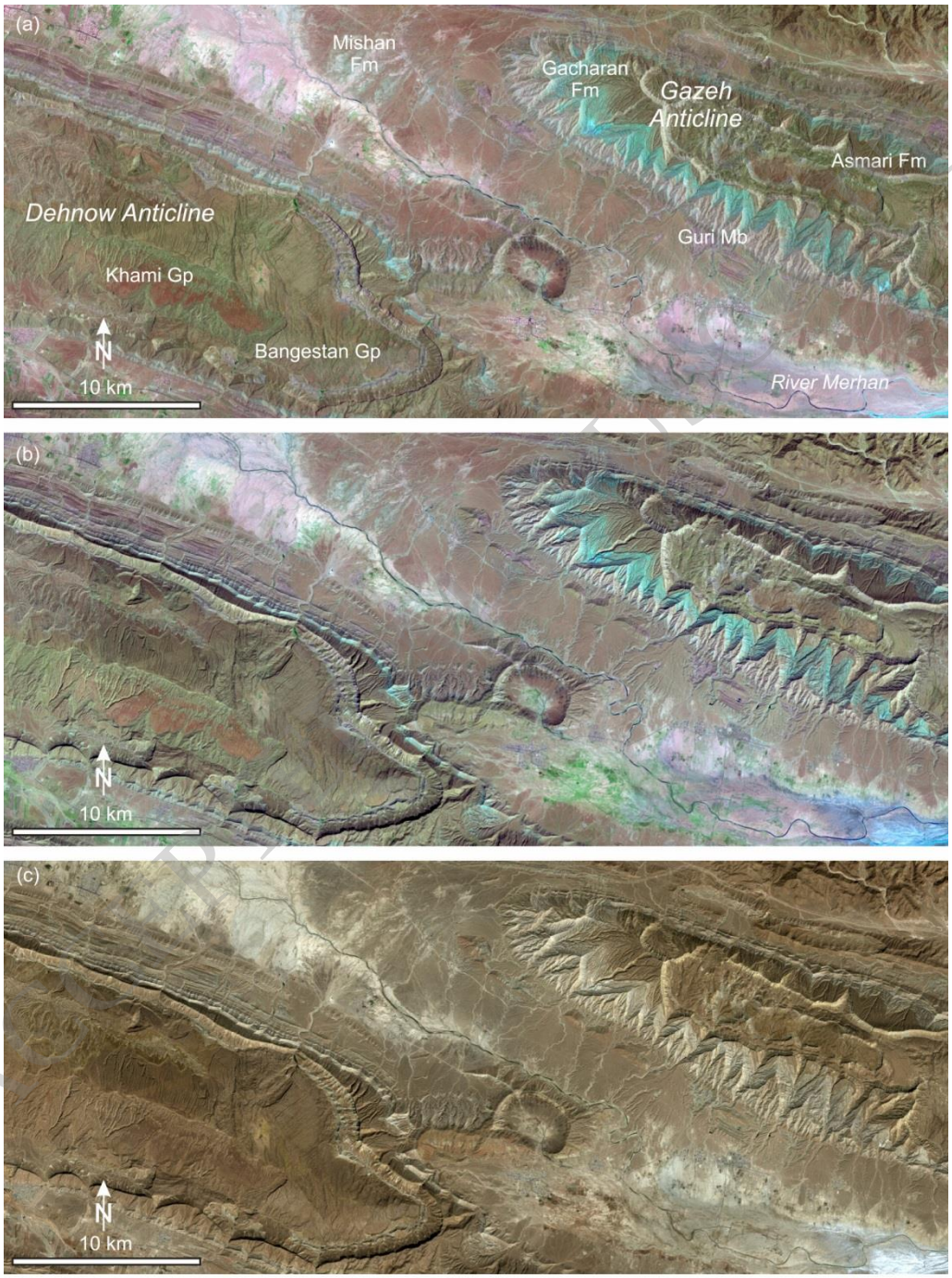

Downloaded from http://sp.lyellcollection.org/ by guest on February 14, 2019

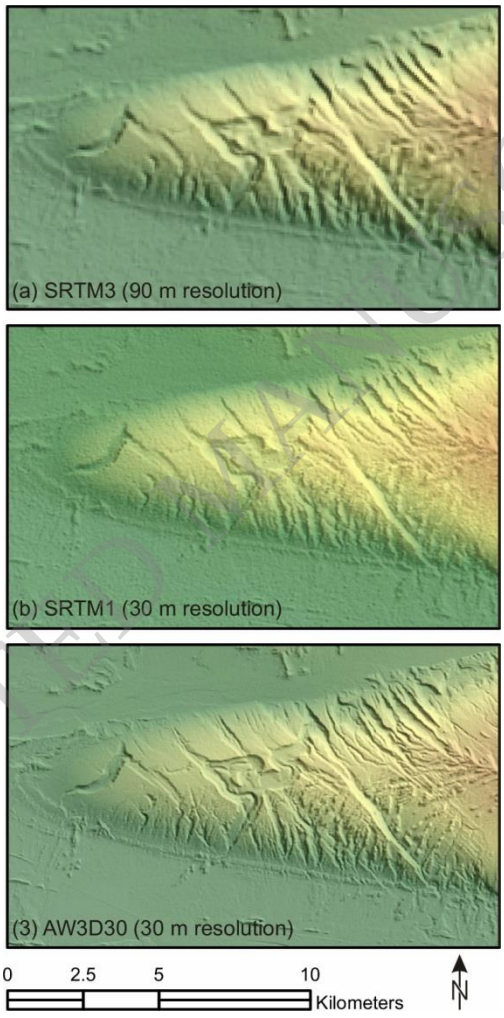

ACCEPTED MANUSCRIPT

Downloaded from http://sp.lyellcollection.org/ by guest on February 14, 2019

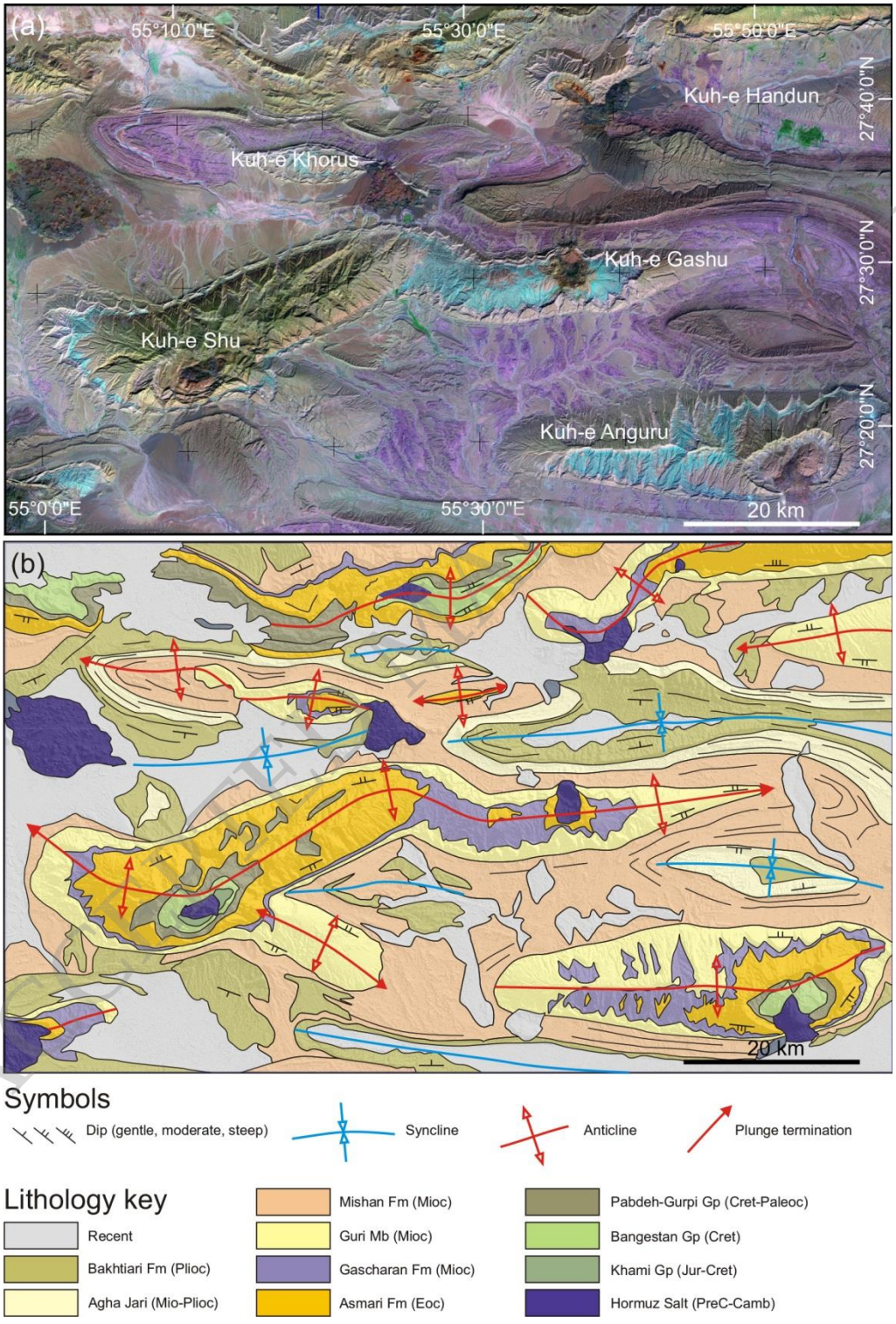

Downloaded from http://sp.lyellcollection.org/ by guest on February 14, 2019

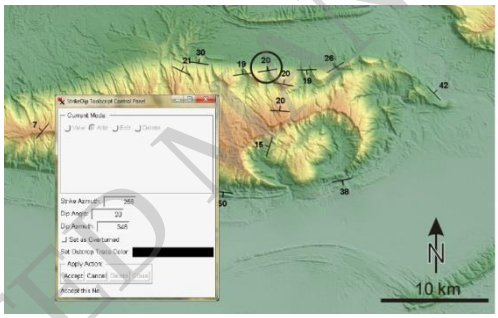

ACCEPTED MANUSCRIPT

Downloaded from http://sp.lyellcollection.org/ by guest on February 14, 2019

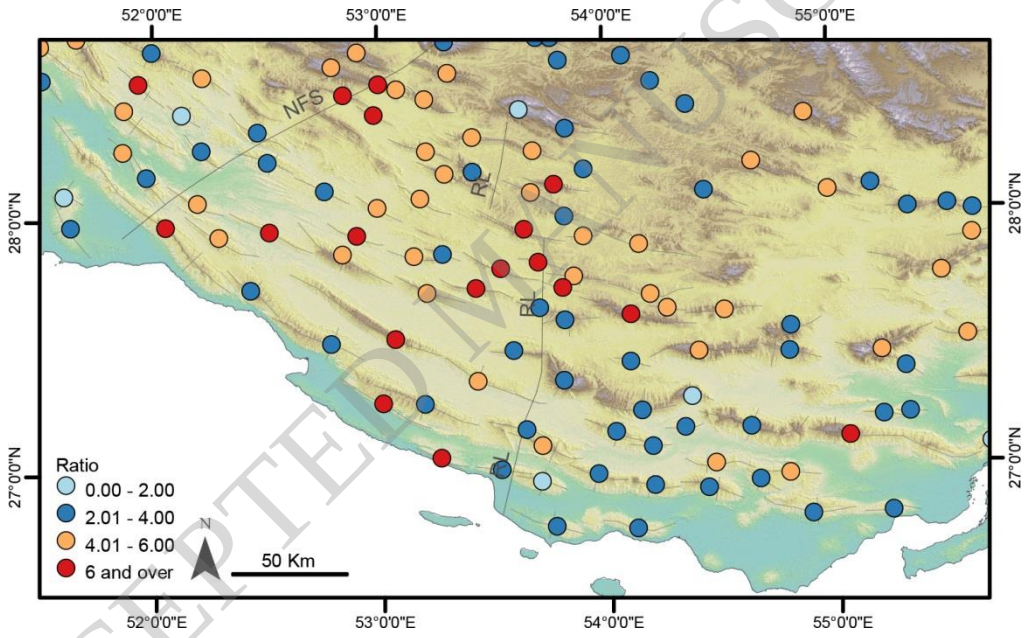

ACCEPTED MANUSCRIPT

Downloaded from http://sp.lyellcollection.org/ by guest on February 14, 2019

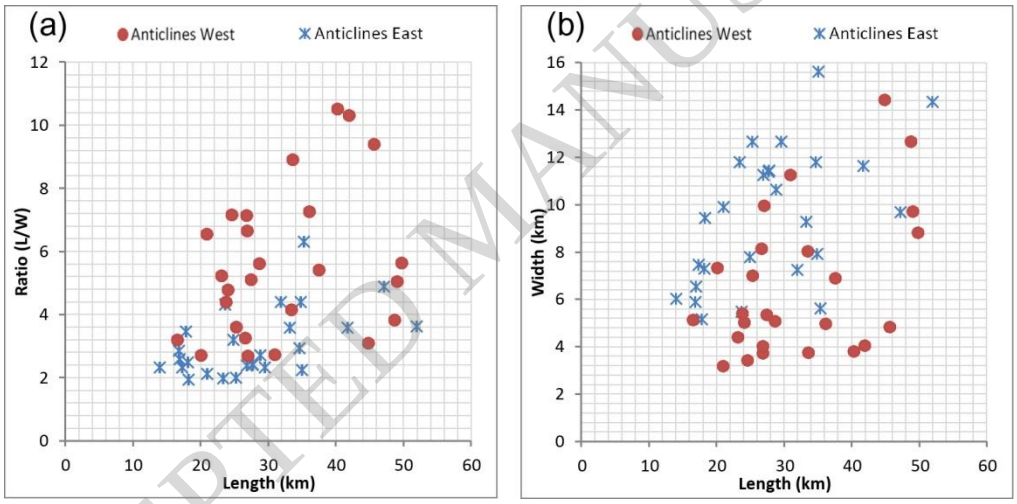

ACCEPTED MANUSCRIPT

Downloaded from http://sp.lyellcollection.org/ by guest on February 14, 2019

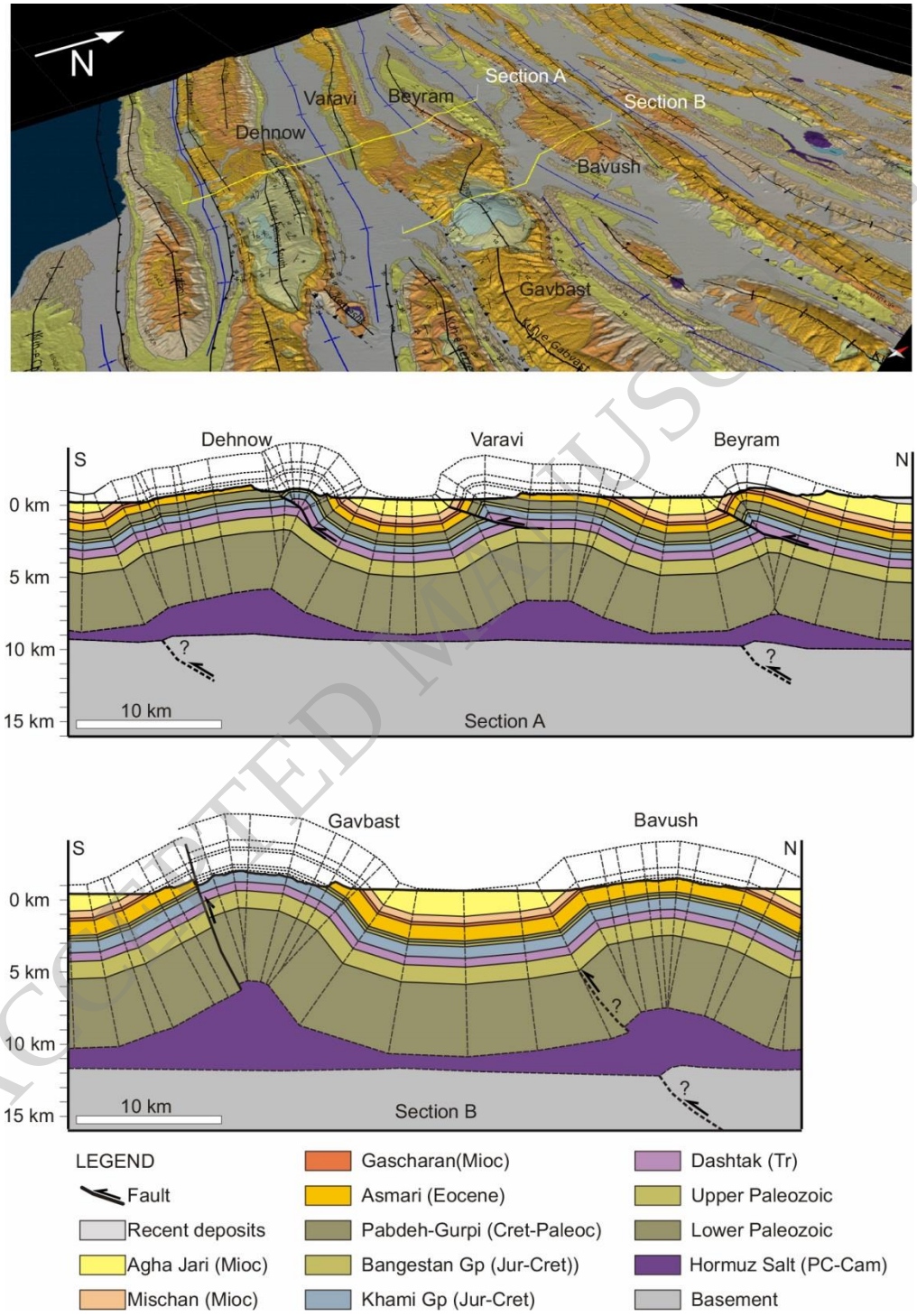

ACCEPTED MANUSCRIPT

Downloaded from http://sp.lyellcollection.org/ by guest on February 14, 2019

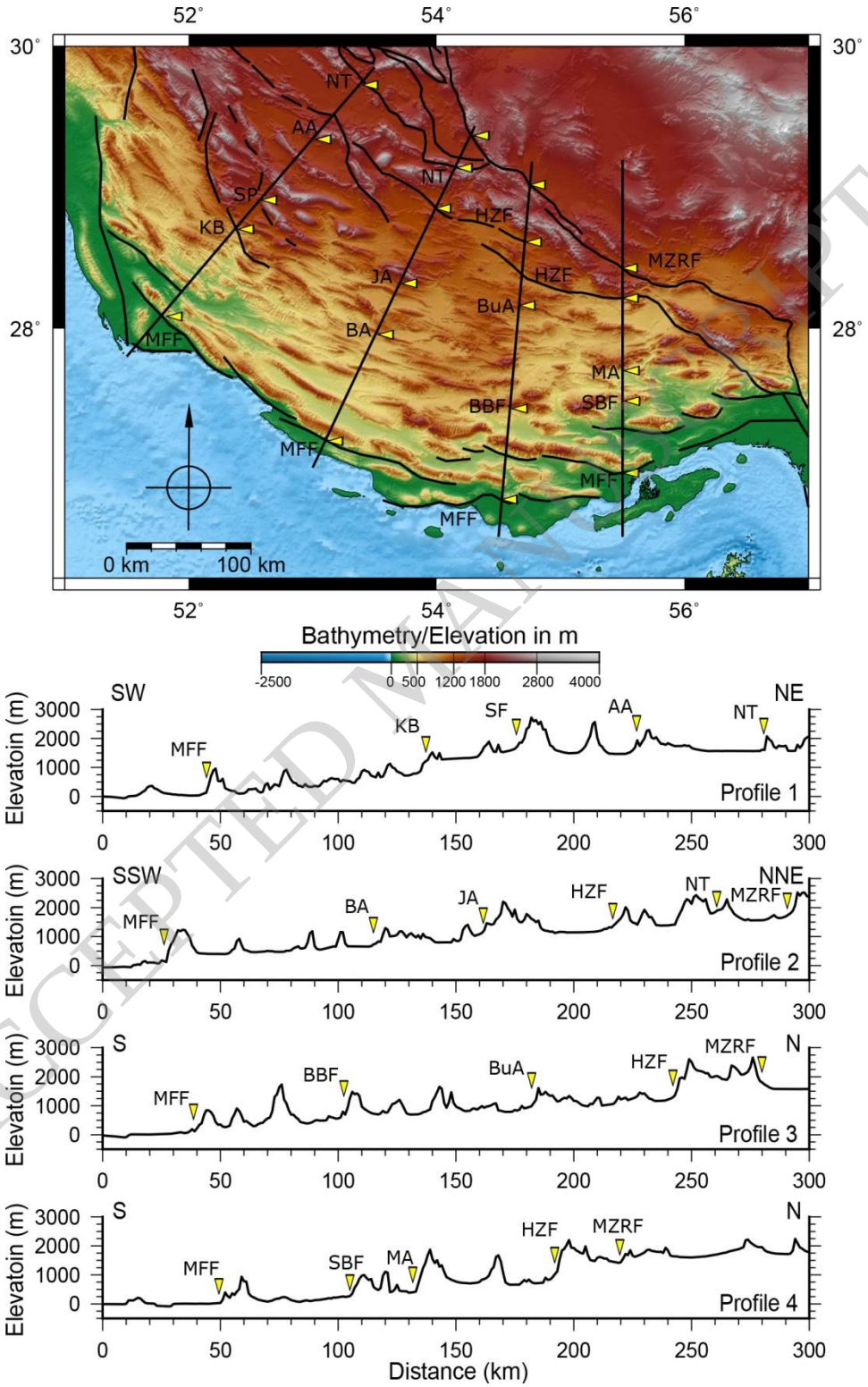

ACCEPTED MANUSCRIPT

Downloaded from http://sp.lyellcollection.org/ by guest on February 14, 2019

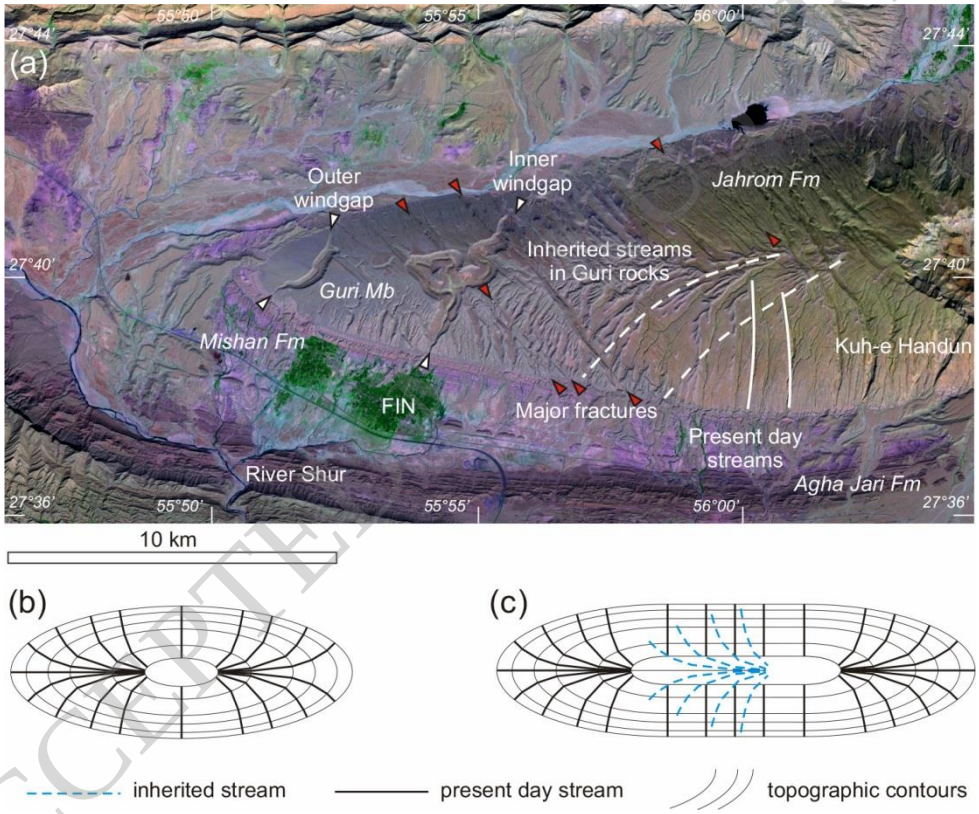

ACCEPTED MANUSCRIPT

Downloaded from http://sp.lyellcollection.org/ by guest on February 14, 2019

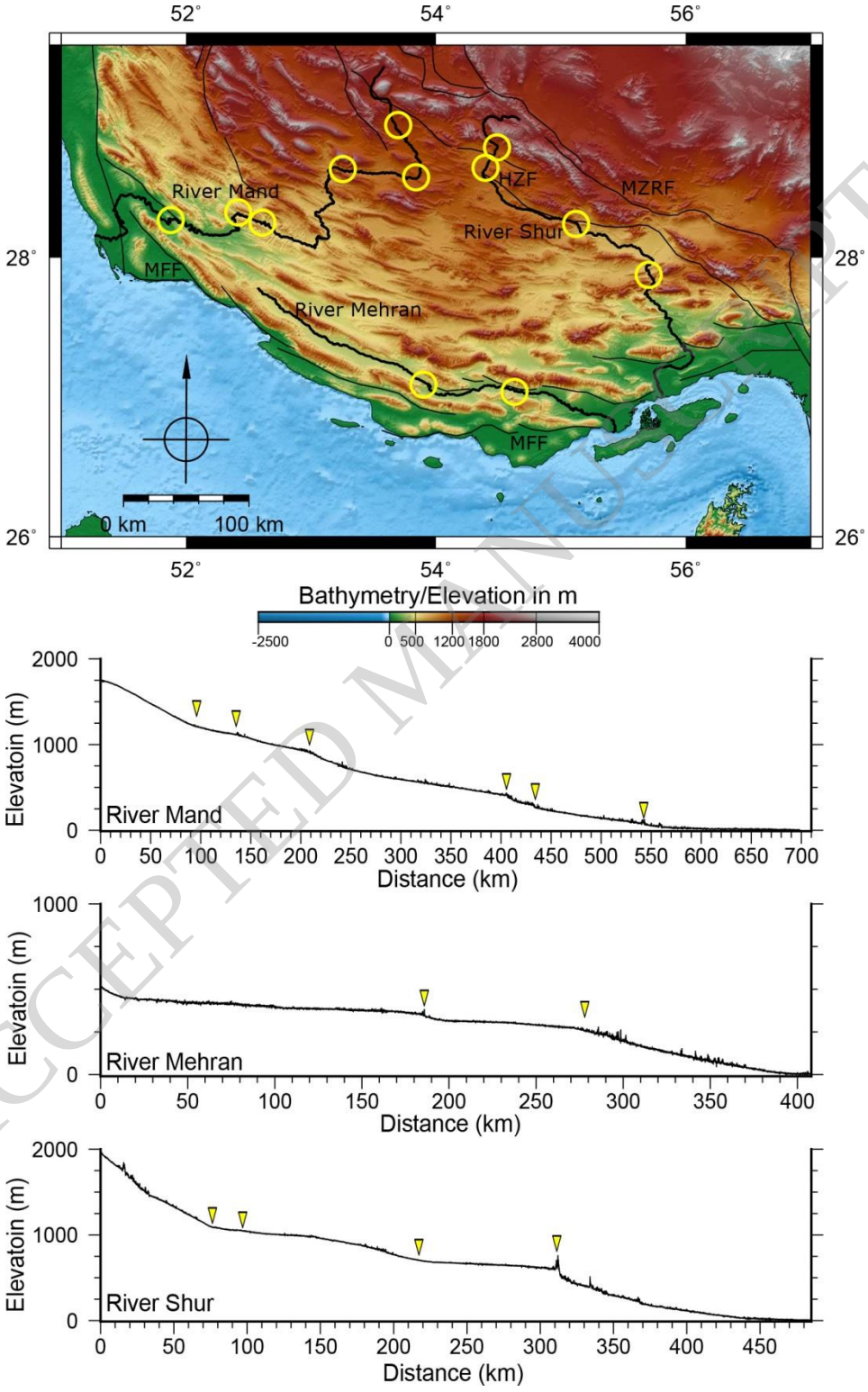

ACCEPTED MANUSCRIPT

Downloaded from http://sp.lyellcollection.org/ by guest on February 14, 2019

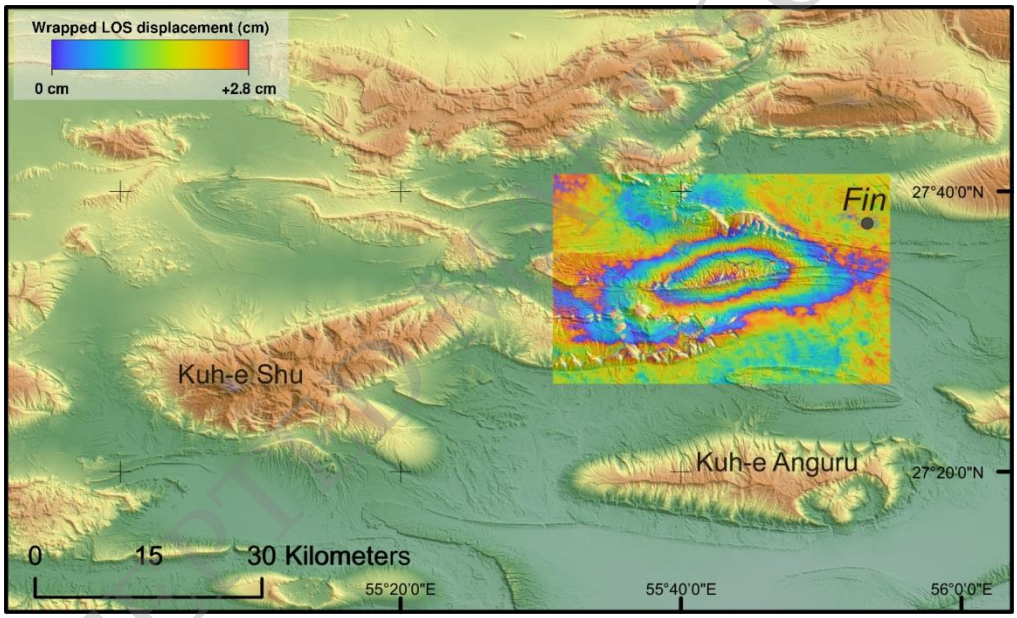

ACCEPTED MANUSCRIPT

Downloaded from http://sp.lyellcollection.org/ by guest on February 14, 2019

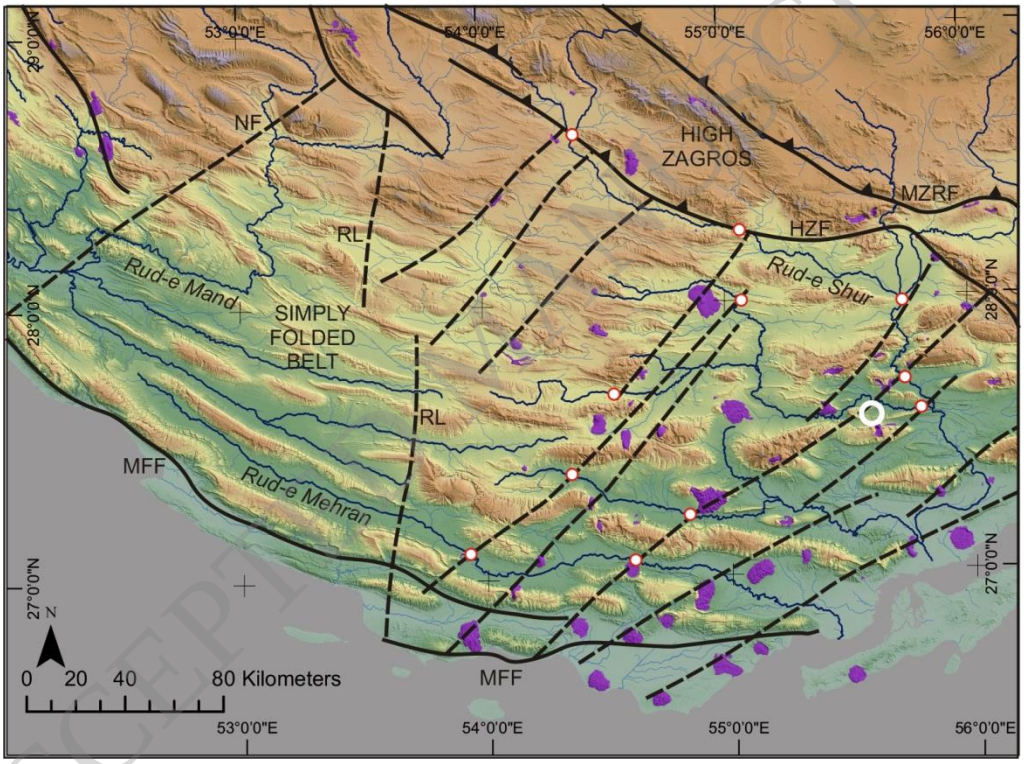

ACCEPTED MANUSCRIPT